

Theoretical Transmission Spectra of Exoplanet Atmospheres with Hydrocarbon Haze:
Effect of Creation, Growth, and Settling of Haze Particles. II.
Dependence on UV Irradiation Intensity, Metallicity, C/O Ratio, Eddy Diffusion Coefficient, and Temperature

YUI KAWASHIMA^{1,2,3} AND MASAHIRO IKOMA^{3,4}

¹*SRON Netherlands Institute for Space Research, Sorbonnelaan 2, 3584 CA Utrecht, The Netherlands*

²*Earth-Life Science Institute, Tokyo Institute of Technology 2-12-1-IE-1 Ookayama, Meguro-ku, Tokyo 152-8550, Japan*

³*Department of Earth and Planetary Science, Graduate School of Science, The University of Tokyo, 7-3-1 Hongo, Bunkyo-ku, Tokyo 113-0033, Japan*

⁴*Research Center for the Early Universe (RESCEU), Graduate School of Science, The University of Tokyo, 7-3-1 Hongo, Bunkyo-ku, Tokyo 113-0033, Japan*

(Received; Revised; Accepted)

Submitted to ApJ

ABSTRACT

Recent transmission spectroscopy has revealed that clouds and hazes are common in the atmospheres of close-in exoplanets. In this study, using the photochemical, microphysical, and transmission spectrum models for close-in warm ($\lesssim 1000$ K) exoplanet atmospheres that we newly developed in our preceding paper (Kawashima & Ikoma 2018), we investigate the vertical distributions of haze particles and gaseous species and the resultant transmission spectra over wide ranges of the model parameters including UV irradiation intensity, metallicity, carbon-to-oxygen ratio (C/O), eddy diffusion coefficient, and temperature. The sensitivity to metallicity is of particular interest. We find that a rise in metallicity leads basically to reducing the photodissociation rates of the hydrocarbons and therefore the haze monomer production rates. This is due to an enhanced photon-shielding effect by the major photon absorbers such as H₂O, CO, CO₂, and O₂, existing at higher altitudes than the hydrocarbons. We also find that at relatively short wavelengths ($\lesssim 2\text{--}3\ \mu\text{m}$), the absorption features in transmission spectra are most pronounced for moderate metallicities such as 100 times the solar metallicity, whereas the lower the metallicity the stronger the absorption features at relatively long wavelengths ($\gtrsim 2\text{--}3\ \mu\text{m}$), where the contribution of haze is small. These are because of the two competing effects of reduced haze production rate and atmospheric scale height for higher metallicities. For the other model parameters, we show that stronger absorption features appear in transmission spectra of the atmospheres with lower UV irradiation, lower C/O ratio, higher eddy diffusion coefficient, and higher temperature.

Keywords: planets and satellites: atmospheres — planets and satellites: composition — planets and satellites: individual (GJ 1214b)

1. INTRODUCTION

Multi-wavelength simultaneous observations have been done for transits of several exoplanets. A set of transit depths thus observed is termed a transmission spectrum. It provides information of radiative absorption and scattering by gaseous molecules and particles

such as haze and clouds in the planetary atmosphere¹. Thus, comparison between observational and theoretical transmission spectra can constrain the properties of the planetary atmosphere. Recent multi-wavelength transit observations have revealed that many of those observed planets show spectra with steep slope features in the

Corresponding author: Yui Kawashima
y.kawashima@sron.nl

¹ In this study, we refer to thermochemical condensates as “clouds” and photochemical products as “haze”.

visible and/or featureless spectra in the near-infrared (e.g., Kreidberg et al. 2014; Sing et al. 2016), inferring the existence of haze and/or clouds in the atmospheres, which prevents us from probing the atmospheric molecular composition.

As for planets with hydrogen-rich atmospheres orbiting M stars, which will be the main targets for near-future exoplanet characterization, hydrocarbon haze has attracted particular interest from the exoplanetary science community as a likely candidate for particles in relatively cool atmospheres. (In this study, we also refer to organic haze as hydrocarbon haze.) While previous theoretical modeling of transmission spectra of such atmospheres (e.g., Howe & Burrows 2012; Morley et al. 2013; Ehrenreich et al. 2014) made ad hoc assumptions about the properties of the haze layer (namely, the size and number density of haze particles and the altitude and thickness of the haze layer), recent studies (Lavvas & Koskinen 2017; Kawashima & Ikoma 2018; Kawashima et al. 2019) considered the microphysics of particles, namely, collisional growth, sedimentation, and transport by eddy diffusion and thereby determined the distribution of the size and number density of haze particles directly. Such microphysical modeling has been also applied to condensation clouds to derive their distributions in exoplanet atmospheres recently (Ohno & Okuzumi 2018; Powell et al. 2018; Gao & Benneke 2018; Ormel & Min 2019).

In our preceding paper (Kawashima & Ikoma 2018, hereafter Paper I), we developed new photochemical and microphysical models of the creation, growth, and settling of haze particles for deriving their size and number-density distributions in atmospheres of close-in warm ($\lesssim 1000$ K) exoplanets. We also developed radiative extinction models for generating theoretical transmission spectra of the atmospheres, combined with obtained properties of haze. In Paper I, we focused on describing the methodology and demonstrating the sensitivity of transmission spectra to the production rate of haze monomers. We found that the haze was distributed in the atmosphere much more broadly than previously assumed and consisted of particles of various sizes. We also demonstrated that differences in production rate of haze monomers, which is related to UV irradiation intensity from host stars, could explain the observed diversity of transmission spectra; completely flat spectrum, spectrum with only extinction features of hazes (i.e., a spectral slope due to Rayleigh scattering and absorption features of hazes), spectrum with a slope due to Rayleigh scattering and some molecular absorption features, and spectrum with only molecular absorption features.

In this paper, we make a detailed investigation of the dependence of transmission spectra on model parameters, namely, UV irradiation intensity, metallicity, carbon-to-oxygen ratio (C/O), eddy diffusion coefficient, and atmospheric temperature for close-in warm ($\lesssim 1000$ K) exoplanets, adopting a more realistic assumption for haze monomer production rate than in Paper I. From this investigation, we explore possible combinations of the model parameters that result in larger or smaller absorption features in the transmission spectra, aiming to provide a strategy for future observations. Such an exploration has been done for hot Jupiters by Lavvas & Koskinen (2017), but not yet for warm super-Earths. In our forthcoming papers, we explore in detail the composition of the atmospheres of known warm exoplanets by comparing the observed spectra with our theoretical ones.

The rest of this paper is organized as follows: In §2, we briefly describe our photochemical, particle growth, and transmission spectrum models. In §3, we show the dependence of the distributions of gaseous species and haze particles and transmission spectra on the above model parameters. Then, we discuss implications for observations, those from experiments, comparison with previous studies, and caveats in §4 and finally conclude this paper in §5.

2. METHOD

We outline our modeling of transmission spectra of an atmosphere with hydrocarbon haze as follows: First, we perform photochemical calculations to derive the steady-state vertical distribution of gaseous species for a given temperature distribution in the atmosphere (§ 2.1). Then, we define the production rate of the smallest-size haze particles (called haze monomers, hereafter) as the sum of the photodissociation rates of the major hydrocarbons included in our photochemical calculations such as CH_4 , HCN , and C_2H_2 . After that, using the profile of the haze-monomer production rate, we derive the steady-state distribution of haze particles by the particle growth calculations (§ 2.2). Finally, we model transmission spectra of the atmospheres with the obtained distributions of haze particles and gaseous species (§ 2.3).

Same as in Paper I, we model the transmission spectra, assuming the properties of GJ 1214 b, the atmosphere of which has been probed most by transmission spectroscopy observations among super-Earths detected so far.

The photochemical, particle growth, and transmission spectrum models used in this study are basically the same as those developed and described in Paper I. Below, we briefly describe our models and explain the as-

sumptions and parameters we adopt, with focus on differences from Paper I.

2.1. Photochemical Model

Our photochemical model includes five elements, C, H, O, N, and He, 29 chemical species, O, O₂, H₂O, H, OH, CO₂, CO, HCO, CH₄, CH₃, CH₃O, CH₃OH, CH, CH₂, C, C₂, C₂H, C₂H₂, N, N₂, NH, NH₂, NH₃, CN, HCN, H₂, He, O(¹D), and ¹CH₂. It contains 154 thermochemical reactions (and their reverse reactions) and 16 photochemical reactions, which are listed in Tables 1 and 2 of Paper I, respectively.

For the boundary conditions, we assume the diffusion fluxes of all the species to be zero at the upper boundary and the volume mixing ratios of gaseous species to be the thermochemical equilibrium values at the lower boundary.

We prepare 165 atmospheric layers with same thickness Δz . We place the lower boundary at 1000 bar and set the thickness Δz to 45 km except for the cases of 10, 100, and 1000 times the Solar metallicity, for which $\Delta z = 40, 18, \text{ and } 4 \text{ km}$, respectively, (see § 3.3), and the case with the irradiation temperature $T_{\text{irr}} = 1290 \text{ K}$, for which $\Delta z = 100 \text{ km}$ (see § 3.6).

2.2. Particle Growth Model

We derive the steady-state number density of haze particles of various sizes at each altitude, considering the collisional growth, sedimentation, transport by eddy diffusion, and monomer production. As for collisional growth, we consider two processes, the Brownian diffusion and gravitational collection. The latter is the collisional process that occurs as a result of the difference in sedimentation velocity between different-size particles. We neglect the effect of thermal decomposition, which Lavvas & Koskinen (2017) considered, since it does not occur in the pressure and temperature ranges considered in this study. Same as in Paper I, we prepare 40 volume bins, setting the volume ratio of two adjacent bins to be 3.

In Paper I, as for monomer production, we assumed that the integrated mass of the monomers produced per unit time throughout the atmosphere was equal to the production rate observed in Titan's atmosphere multiplied by the ratio of the incident stellar Ly α flux at the planet's orbital distance to that currently received by Titan. Then, we distributed the production rate according to the distribution of the sum of the number densities of haze precursors, which were assumed to be HCN and C₂H₂, at each altitude. Those are similar assumptions used in the previous studies such as Trainer et al. (2006) and Morley et al. (2013). Instead, in this study, we define the monomer production rate at each altitude as

the sum of the photodissociation rate of CH₄, HCN, and C₂H₂ as is a more realistic assumption. Thus, the production rate of monomers at altitude z , $p(v_1, z)$, is given as a function of the monomer volume v_1 and mass $m_{p,1}$,

$$p(v_1, z) = \frac{\sum_i^{\text{CH}_4, \text{HCN}, \text{C}_2\text{H}_2} m_i J_i(z) n_i(z)}{m_{p,1}}, \quad (1)$$

where m_i , J_i , and n_i are the mass, photodissociation rate (the number of molecules dissociated per unit time), and number density of molecule i , respectively.

As for the boundary conditions, we consider that all the particles are lost at the lower boundary at a rate corresponding to the larger of the sedimentation velocity and the downward velocity imposed by the atmospheric mixing, following Lavvas et al. (2010). As the upper boundary conditions, we set zero fluxes for all the particle sizes. We set the lower and upper boundaries at the pressure levels of 10 bar and $1 \times 10^{-10} \text{ bar}$, respectively, and divide the atmosphere in that pressure range into 200 layers of same thickness.

2.3. Transmission Spectrum Model

We use exactly the same method to model the transmission spectra as the one we used in Paper I. This modeling had been already applied to WASP-80b in Fukui et al. (2014) and for HAT-P-14b in Fukui et al. (2016).

We assume that all the parts of the sphere inside the 10 bar level are optically thick enough to block the incident stellar light completely. This assumption is valid, since we have confirmed that the chord optical depth at the pressure level of 10 bar is sufficiently larger than unity in the atmosphere considered in this study. We calculate the opacity and transit depth over a wavenumber grid with a width of 0.1 cm^{-1} .

We use the bhmie code (Bohren & Huffman 2004) to calculate the extinction opacity of haze particles. As for the complex refractive indices of haze, we use the experimental values of tholin from Khare et al. (1984). Note that since these are the laboratory-experimental values in a simulated Titan's atmospheric composition of 0.9N₂/0.1CH₄ gas mixture, the complex refractive indices of haze in atmospheres of different composition such as ones of interest in this study can be different. In Figure 1, we show the extinction cross sections of the haze particles of five different particle radii, namely, 0.001, 0.01, 0.1, 1, and 10 μm , which are smoothed with the resolution of $R = 100$. Note that the bumps found around 3.0 and 4.6 μm come from the vibrational transitions of the C-H bond and C \equiv N bond of the tholin-like haze particles, respectively (Khare et al. 1984).

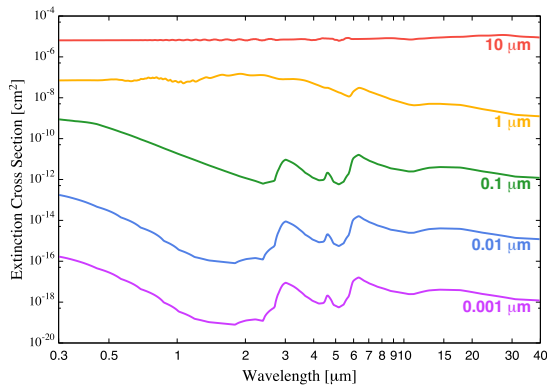


Figure 1. Extinction cross sections of the tholin-like haze particles of five different particle radii of 0.001, 0.01, 0.1, 1, and 10 μm , which are smoothed with the resolution of $R = 100$. Note that this figure is the same as Figure 1 of Paper I, but extended to longer wavelengths.

For the opacities of gaseous molecules, we consider line absorption by H_2O , CO_2 , CO , CH_4 , O_2 , NH_3 , OH , N_2 , HCN , C_2H_2 , and H_2 , taking their line data from HITRAN2012 (Rothman et al. 2013) in addition to their Rayleigh scattering and the collision-induced absorption by $\text{H}_2\text{-H}_2$ and $\text{H}_2\text{-He}$. We ignore the Rayleigh scattering by OH , because of its low abundance in the atmosphere and thus negligible effect.

2.4. Model Setting and Input Parameters

As described in Introduction, this study is aimed at exploring the sensitivity of the haze particle distribution and transmission spectrum especially to UV irradiation intensity, metallicity, carbon-to-oxygen ratio (C/O), eddy diffusion coefficient, and temperature in the atmosphere. Here, we explain the model setting and input parameters.

We use observed properties of GJ1214 b and its host star: The stellar radius is $0.201 R_\odot$ (Anglada-Escudé et al. 2013). The planetary mass is $6.26 M_\oplus$ (Anglada-Escudé et al. 2013). We choose $2.07 R_\oplus$ as the planetocentric distance at 1000 bar so as to roughly match the observed transit radii of GJ 1214 b with the assumption of a clear solar-composition atmosphere and use this value for all the atmospheric scenarios presented in this paper. Note that when we investigate atmospheric compositions from observed transit depths, we often suffer from degeneracy among the reference radius and those inferred properties (e.g., Heng & Kitzmann 2017). Relative values of transit depths at different wavelengths rather than the absolute ones are useful for constraining the atmospheric properties.

As for the stellar UV spectrum, same as in Paper I, we use the GJ 1214’s spectrum constructed by the MUSCLES Treasury Survey (France et al. 2016;

Youngblood et al. 2016; Loyd et al. 2016). We adopt its version 1.1 of the panchromatic SED binned to a constant 1 \AA resolution and downsampled in low signal-to-noise regions to avoid any negative flux. Unlike in Paper I, however, in this study, we adopt 8 \AA resolution since we have confirmed that this resolution is sufficient for our calculations. We derive the 8 \AA resolution spectrum by averaging the original data points within the wavelength range of the resolution. When we explore the sensitivity to UV irradiation intensity in § 3.2, we vary the intensities of the incoming stellar UV flux at all the wavelengths.

The elemental abundance ratios for the fiducial case are assumed to be equal to the solar system abundance ratios, which we take from Table 2 of Lodders (2003). That corresponds to C/O, O/H, and N/H of 5.010×10^{-1} , 5.812×10^{-4} , and 8.021×10^{-5} , respectively. When we consider high metallicity cases including 10, 100, and 1000 times the Solar metallicity in § 3.3, we enhance the abundances of all the elements except H and He by a factor of 10, 100, and 1000, respectively. The mass proportions of all the elements except H and He for the cases of 1, 10, 100, and 1000 times the Solar metallicity are $Z = 9.89 \times 10^{-3}$, 9.08×10^{-2} , 0.500, and 0.909, respectively. When we explore the sensitivity to the C/O ratio (i.e., 1, 10, and 1000 times the Solar C/O ratio) in § 3.4, we change its value, keeping the ratio of the sum of C and O abundances to the other element abundances unchanged.

As for the eddy diffusion coefficient K_{zz} , we set its fiducial value to be $1 \times 10^7 \text{ cm}^2 \text{ s}^{-1}$. In addition, we explore the cases of $K_{zz} = 1 \times 10^9$ and $1 \times 10^5 \text{ cm}^2 \text{ s}^{-1}$ in § 3.5.

For the temperature-pressure profile, same as in Paper I, we use the analytical formula of Eq. (29) of Guillot (2010). We choose the fiducial values of the parameters, namely, the intrinsic temperature T_{int} , irradiation temperature T_{irr} , averaged opacity in the optical k_v , and that in the infrared k_{th} so as to match the temperature-pressure profile of GJ 1214b that Miller-Ricci & Fortney (2010) derived for a solar composition atmosphere under the assumption of efficient heat redistribution from the day and night sides. This yields $T_{\text{int}} = 120 \text{ K}$, $T_{\text{irr}} = 790 \text{ K}$, $k_v = 10^{-4.1} \text{ cm}^2 \text{ g}^{-1}$, and $k_{\text{th}} = 10^{-2.7} \text{ cm}^2 \text{ g}^{-1}$ ². Even when we consider the atmosphere with elemen-

² Note that the values of k_v and k_{th} are slightly different from those used in Paper I, in which $k_v = 10^{-4.0} \text{ cm}^2 \text{ g}^{-1}$ and $k_{\text{th}} = 10^{-2.6} \text{ cm}^2 \text{ g}^{-1}$. This difference comes from the method used to solve the equation of hydrostatic equilibrium. We used a first-order (Euler) integration method in Paper I, but use the fourth-order (Runge-Kutta) method in this study. We have confirmed that the difference coming from the different choice of k_v

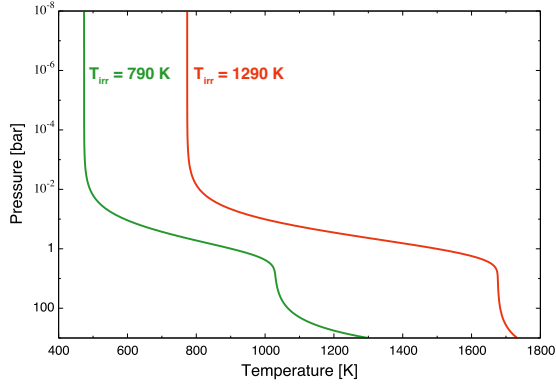


Figure 2. Temperature-pressure profiles of the atmosphere that we use to explore the dependence on temperature in § 3.6. The green line represents the fiducial profile, which is calculated by the use of the analytical formula of Guillot (2010). Also shown is the profile for the irradiation temperature T_{irr} higher by 500 K than the fiducial value of 790 K, namely 1290 K, (red line) with the other parameters unchanged from the fiducial values.

tal abundance ratios other than the solar ones, we use the same parameters, since the focus of this study is on the effect of elemental abundance ratios. In § 3.6, we explore the case where T_{irr} is higher by 500 K than the fiducial value of 790 K, namely 1290 K, keeping the other parameters unchanged from the fiducial values to investigate the dependence on temperature. Figure 2 shows the temperature-pressure profiles of the atmosphere that we use as the fiducial (green line) and higher- T_{irr} cases, which we use in § 3.6.

Finally, as for the monomer radius, we adopt 1 nm. Thus, radius bins range from 1 nm to 1600 μm . We have confirmed it has a little effect on transmission spectra. A brief discussion is made in § 4.4.1. For the value of the material density of haze particles, we adopt 1.0 g cm^{-3} as the widely used value for the microphysical models of Titan’s haze (e.g., Toon et al. 1992; Lavvas et al. 2011). We also make a brief discussion on this effect in § 4.4.2.

3. RESULTS

In this section, we present the results of our numerical simulations. First, we overview the distributions of gaseous species and haze particles and transmission spectra that we obtain in the fiducial case in § 3.1. Then, we explore the dependence of the transmission spectra on UV irradiation intensity in § 3.2, metallicity in § 3.3,

and k_{th} has little effect on our results and conclusions of Paper I, as realized by comparison between Figure 2 of Paper I and Figure 3(a) of this paper (the differences being in the value of k_v and k_{th} , the integration method for the equation of hydrostatic equilibrium, and the resolution of the input stellar spectrum only.)

C/O ratio in § 3.4, eddy diffusion coefficient in § 3.5, and temperature in § 3.6.

3.1. Fiducial Case

3.1.1. Photochemistry and Haze Precursor Production

In Figure 3, we show the results of our photochemical calculations for the fiducial case. Although these results are basically the same as those of § 3.1 of Paper I, we show them because they are helpful in interpreting our later results. Figure 3 (a) shows the calculated vertical distributions of gaseous species in the photochemical equilibrium state (solid lines). For reference, we also present the distributions obtained by thermochemical equilibrium calculations (dashed lines) that ignore photochemical processes and eddy diffusion transport. In the lower atmosphere ($P \gtrsim 10^{-4}$ bar), NH_3 , N_2 , and CO are found to have constant values of the volume mixing ratio equal to their lower boundary values because of the eddy diffusion mixing. In the upper atmosphere ($P \lesssim 10^{-4}$ bar), many species that hardly exist in thermochemical equilibrium (i.e., H, O, C, HCN, N, O_2 , C_2H_2 , CH_3 , OH, CH_3OH , NH_2 , CH_2 , and $\text{O}(^1\text{D})$) are produced due to photochemical reactions, and H is the most abundant species.

In Figure 3 (b), we plot the vertical profile of the photodissociation rate of each species, namely, the number of molecules that photodissociate per unit volume and unit time. Note that the photodissociation rate of O_2 (light blue) just above the lower boundary (1000 bar) is calculated from its volume mixing ratio whose value is out of our computational precision, so that its value is physically meaningless. One finds that H_2 , CO , H_2O , and NH_3 make major contribution to absorption of stellar photons via photodissociation. Among the haze precursors (CH_4 , HCN, and C_2H_2), C_2H_2 photodissociates most in spite of the lowest abundance. This is because C_2H_2 can use photons of low-energy, namely, incoming stellar flux at long wavelengths (up to ~ 220 nm), for its photodissociation, unlike the other two molecules. Therefore, in our simulations, C_2H_2 makes the greatest contribution to the haze monomer production. Also, in Table 1, we tabulate the photodissociation rates of the haze precursors integrated over the calculation range of pressure in our particle growth simulations, between 10^{-10} and 10 bar. The sum of the photodissociation rates of these haze precursors (the 6th column of the table) is assumed as the monomer production rate in the particle growth simulations.

3.1.2. Particle Growth

Figure 4 shows the calculated vertical profiles of haze properties. Here, we define the volume average radius

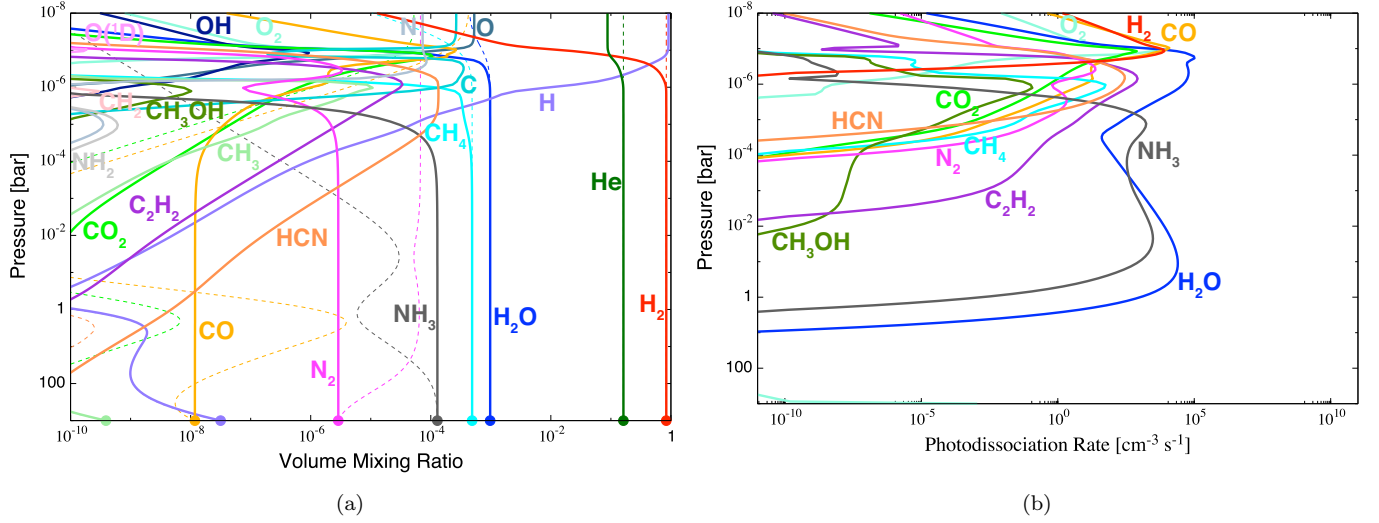


Figure 3. Photochemical properties of the atmosphere for the fiducial case. (a) Vertical distributions of gaseous species in photochemical equilibrium (solid line). The filled circles represent the thermochemical equilibrium values at the lower boundary. For reference, shown by the dashed lines are the abundances in thermochemical equilibrium, where the eddy diffusion transport is also ignored. (b) Vertical profile of the photodissociation rate of each species, namely, the number of molecules that photodissociate per unit volume and unit time. Note that Figure (a) is basically the same as Figure 2 of Paper I with the differences being in the value of k_v and k_{th} , the integration method for the equation of hydrostatic equilibrium, and the resolution of the input stellar spectrum only.

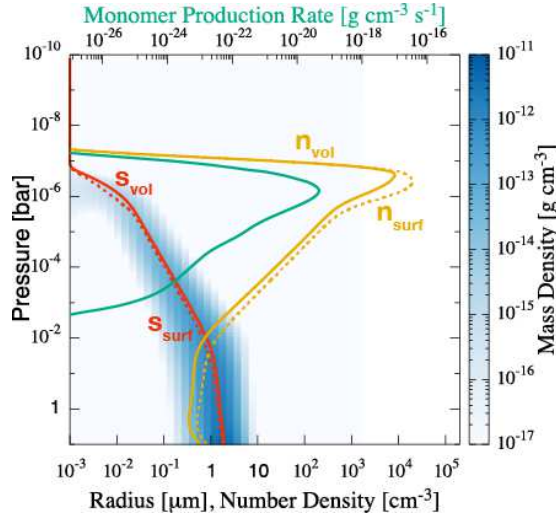


Figure 4. Vertical profiles of the volume average radius s_{vol} (red solid line) and number density n_{vol} (orange solid line), and the surface average radius s_{surf} (red dashed line) and number density n_{surf} (orange dashed line), along with that of the monomer mass production rate (green solid line), for the fiducial case. See the text for the definition of each quantity. The mass densities for all the size bins at each pressure level are also plotted with the blue color contour. Note that the mass density here refers not to material density of haze particles, but to their spatial density.

s_{vol} (red solid line) and surface average radius s_{surf} (red

dashed line), respectively, as

$$s_{vol} = \frac{\sum_{i=1}^{\mathcal{N}} n(s_i) s_i^4}{\sum_{i=1}^{\mathcal{N}} n(s_i) s_i^3}, \quad s_{surf} = \frac{\sum_{i=1}^{\mathcal{N}} n(s_i) s_i^3}{\sum_{i=1}^{\mathcal{N}} n(s_i) s_i^2}, \quad (2)$$

where $n(s_i)$ is the number density of particles with radius s_i and \mathcal{N} is the total number of volume bins used in the calculations. If the two average sizes coincide with each other at a certain altitude, the size distribution is unimodal at the altitude. The volume average number density n_{vol} (orange solid line) and the surface average number density n_{surf} (orange dashed line) are calculated, respectively, as

$$n_{vol} = \frac{\sum_{i=1}^{\mathcal{N}} n(s_i) s_i^3}{s_{vol}^3}, \quad n_{surf} = \frac{\sum_{i=1}^{\mathcal{N}} n(s_i) s_i^3}{s_{surf}^3}. \quad (3)$$

Additionally, the mass densities for all the size bins at each pressure level are plotted with the blue color contour and the vertical profile of the monomer mass production rate is plotted with the green solid line.

In Figure 4, one finds that both average radii increase from 1×10^{-3} to $\sim 2 \mu\text{m}$ via collisional growth. The number densities take their peak values at $\sim 2\text{--}4 \times 10^{-7}$ bar. This is because, below this altitude, the atmospheric pressure is high enough that the collisional growth occurs via the Brownian diffusion rapidly compared to the monomer production. Change of the trend found at $P \sim 10^{-2}$ bar results from the transition in gas drag law from the slip-flow to Stokes-flow regimes (see

Table 1. Integrated photodissociation rates of haze precursors

	Figure	CH ₄	HCN	C ₂ H ₂	Total
Fiducial	Fig. 3 (b)	1.99×10^{-14}	4.07×10^{-13}	9.49×10^{-13}	1.38×10^{-12}
UV $\times 10^5$	Fig. 7 (b)	6.05×10^{-16}	1.02×10^{-12}	5.33×10^{-9}	5.33×10^{-9}
UV $\times 10^{2.5}$	Fig. 7 (d)	1.78×10^{-13}	1.25×10^{-11}	7.69×10^{-11}	8.96×10^{-11}
UV $\times 10^{-2.5}$	Fig. 7 (f)	1.25×10^{-15}	1.86×10^{-15}	1.01×10^{-15}	4.12×10^{-15}
UV $\times 10^{-5}$	Fig. 7 (h)	1.63×10^{-16}	5.34×10^{-19}	3.01×10^{-23}	1.64×10^{-16}
10 \times Solar	Fig. 10 (b)	3.03×10^{-16}	1.17×10^{-13}	3.94×10^{-13}	5.12×10^{-13}
100 \times Solar	Fig. 10 (d)	9.42×10^{-17}	2.37×10^{-14}	1.62×10^{-13}	1.86×10^{-13}
1000 \times Solar	Fig. 10 (f)	1.80×10^{-13}	9.04×10^{-15}	1.00×10^{-20}	1.89×10^{-13}
C/O = 1	Fig. 13 (b)	4.88×10^{-14}	4.59×10^{-13}	2.47×10^{-12}	2.98×10^{-12}
C/O = 10	Fig. 13 (d)	1.90×10^{-13}	5.98×10^{-13}	1.81×10^{-11}	1.89×10^{-11}
C/O = 1000	Fig. 13 (f)	1.64×10^{-13}	5.61×10^{-13}	7.73×10^{-11}	7.80×10^{-11}
$K_{zz} = 1 \times 10^9 \text{ cm}^2 \text{ s}^{-1}$	Fig. 16 (b)	4.12×10^{-13}	5.68×10^{-13}	5.84×10^{-15}	9.86×10^{-13}
$K_{zz} = 1 \times 10^5 \text{ cm}^2 \text{ s}^{-1}$	Fig. 16 (d)	1.71×10^{-14}	3.66×10^{-13}	1.08×10^{-12}	1.46×10^{-12}
$T_{\text{irr}} = 1290 \text{ K}$	Fig. 19 (b)	7.75×10^{-15}	2.23×10^{-13}	2.06×10^{-14}	2.51×10^{-13}

NOTE— Photodissociation rates (in $\text{g cm}^{-2} \text{ s}^{-1}$) of the haze precursors, CH₄, HCN, and C₂H₂, integrated over the calculation range of pressure in our particle growth simulations, namely, between 10^{-10} and 10 bar. The sum of the photodissociation rates of these haze precursors (the 6th column) is assumed as the monomer production rate in the particle growth simulations. Note the unit of photodissociation rate is different from that used in the figures for photodissociation rate profiles. Here "UV $\times n$ " and " $m \times$ Solar" mean the UV irradiation intensity and atmospheric metallicity are n and m times higher than their fiducial values, respectively, C/O is the carbon-to-oxygen abundance ratio, K_{zz} is the eddy diffusion coefficient, T_{irr} is the irradiation temperature. The fiducial values are $m = 1$, $n = 1$, C/O = 0.5, $K_{zz} = 1 \times 10^7 \text{ cm}^2 \text{ s}^{-1}$, and $T_{\text{irr}} = 790 \text{ K}$.

Paper I for the details), increasing the sedimentation velocity and thereby inhibiting collision between particles. The slight difference between s_{vol} and s_{surf} means that the haze contains different size particles at each altitude. The color contour indicates that particles in some narrow range of size are abundant at each altitude.

Here we note that compared to the fiducial case of Paper I, the integrated monomer production rate adopted in Fig. 4 is smaller by a factor ~ 40 and is distributed only in the upper atmosphere. As a result, both the mass density and average radii of the haze particles are slightly smaller and result in the spectrum with more prominent molecular-absorption features as shown in next section (see also Figs. 6 and 9 of Paper I).

3.1.3. Transmission Spectrum Models

Figure 5 shows the transmission spectrum models for the atmosphere with haze (green line) and without haze (black line). The relative cross section of the planetary disk with a radius corresponding to a certain pressure level is presented by horizontal dotted lines from $P = 1 \times 10^{-6}$ bar to 1 bar. Note that the transmission spectrum models are smoothed for clarity with the resolution R

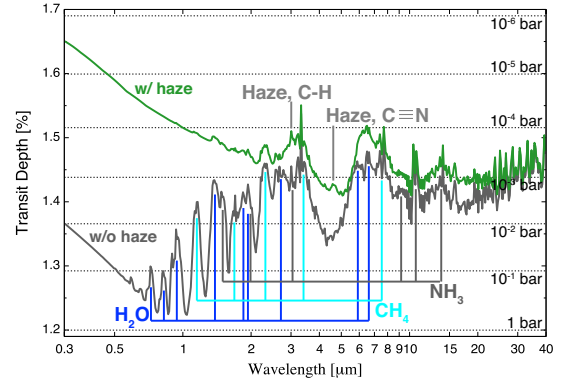


Figure 5. Transmission spectrum models for the atmosphere with haze (green line) and without haze (black line) for the fiducial case. The horizontal dotted lines represent the transit depths corresponding to the pressure levels from 1×10^{-6} bar to 1 bar. Note that the transmission spectrum models are smoothed for clarity with the resolution R of 100.

of 100. We use the same smoothing method for all the spectrum models shown below.

In the spectrum model for the atmosphere without haze (black line), the major spectral features come from

absorption features of H_2O , CH_4 , and NH_3 . Distinct features of H_2O are found around 0.7, 0.8, 0.9, 1.4, 1.8, 1.9, 2.5–2.9, 5.9, and 6.5 μm , those of CH_4 around 1.2, 1.7, 2.3, 3.3, and 7.2–8.4 μm , and those of NH_3 around 1.5, 2.0, 3.0, and 8.4–16.4 μm . The Rayleigh scattering feature mainly due to H_2 can be seen in the optical wavelength region.

The spectrum for the atmosphere with haze (green line) is relatively featureless, compared to that for the atmosphere without haze (black line). This is because the haze particles in the upper atmosphere ($P \lesssim 10^{-3}$ bar) make the atmosphere optically thick and prevent the molecules in the lower atmosphere ($P \gtrsim 10^{-3}$ bar) from showing their absorption features. One finds that the absorption features at shorter wavelengths are more obscured by haze particles, since small haze particles of $\lesssim 1 \mu\text{m}$ floating in the upper atmosphere ($P \lesssim 10^{-3}$ bar) have larger opacity at shorter wavelengths, producing the so-called Rayleigh-scattering slope, and roughly speaking, the optical depth of the clear atmosphere is smaller at shorter wavelengths. The small features of CH_4 above 10^{-3} bar can be seen at 2.3, 3.3, and 7.2–8.4 μm , those of H_2O at 2.5–2.9 and 5.9 μm , and those of NH_3 at 8.4–16.4 μm . Also, the spectral features of the haze particles appear at 3.0, 4.6, and 6.3 μm , respectively.

3.2. Dependence on UV Irradiation Intensity

When exploring the dependence of the transmission spectra on UV irradiation intensity in Paper I, we defined the monomer production rate on the assumption similar to those adopted in Trainer et al. (2006) and Morley et al. (2013). In this paper, more realistically, we define the monomer production rate as the sum of the photodissociation rate of the hydrocarbons CH_4 , HCN , and C_2H_2 (see § 2.2).

Figure 6 shows the transmission spectrum models with haze for different nine choices of the UV irradiation intensity. From this figure, we realize that the transmission spectrum varies significantly with the UV irradiation intensity. This is because the monomer production rate becomes higher with increasing UV irradiation intensity (see § 3.2.1). In the $\text{UV} \times 10^5$ case (red line), the spectrum is characterized by flatness broadly in the infrared and by a Rayleigh-scattering slope in the optical. The former is due to the relatively large ($\sim 0.1 \mu\text{m}$) haze particles floating at high altitudes ($P \sim 10^{-5}$ bar), while the latter is due to the smaller haze particles at higher altitudes (see § 3.2.2). In the $\text{UV} \times 10^{2.5}$ case (yellow line), the absorption features of the haze can be seen at 3.0, 4.6, and 6.3 μm in addition to the Rayleigh scattering in the optical. It is notable that the transit depths in

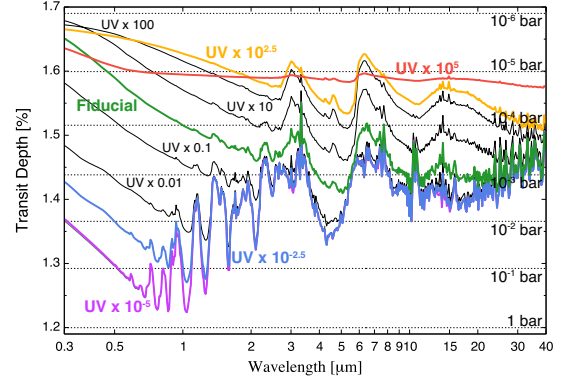


Figure 6. Transmission spectrum models for the atmosphere with haze for different nine choices of UV irradiation intensity: 10^5 (red line), $10^{2.5}$ (yellow line), 100, 10, 0.1, 0.01 (all represented by black thin lines), $10^{-2.5}$ (blue line), and 10^{-5} (purple line) times the fiducial value (green line, same as the green line in Figure 5). All the lines except the fiducial one are labeled “UV $\times n$ ” ($n = 10^5, 10^{2.5}, 100, 10, 0.1, 0.01, 10^{-2.5}, 10^{-5}$). The haze-free transmission spectrum for the atmosphere without haze for the fiducial UV intensity is also plotted (black line, same as the black line in Fig. 5), but can be hardly seen because it overlaps with that for the atmosphere with haze in the case of $\text{UV} \times 10^{-5}$ (purple line). As in Fig. 5, horizontal dotted lines represent the transit depths corresponding to the pressure levels from 1×10^{-6} bar to 1 bar for the atmosphere in the fiducial UV case. Note that the transmission spectrum models are smoothed for clarity.

the optical and at 3.0 and 6.3 μm (i.e., haze absorption features) are larger than those in the $\text{UV} \times 10^5$ case, in spite of the smaller monomer production rate. This is because the monomer production occurs at higher altitudes for lower UV irradiation intensities as shown below and also, the opacities of haze particles at these wavelengths are large. As the UV irradiation intensity decreases, the overall transit depth becomes smaller and the molecular-absorption features become more prominent. In the $\text{UV} \times 10^{-5}$ case (purple line), the spectrum is almost the same as that for the atmosphere without haze (black line). Note that since the monomer production rate assumed here is slightly smaller than that in Paper I, the transmission spectrum models for the same UV irradiation intensity have more distinct Rayleigh scattering slope and/or absorption features, as found by comparison with Figure 14 of Paper I.

3.2.1. Photochemistry and Haze Precursor Production

In Figure 7, we show the calculated vertical distributions of volume mixing ratios (left column) and photodissociation rates (right column) of gaseous species for the cases of $\text{UV} \times 10^5$, $\text{UV} \times 10^{2.5}$, $\text{UV} \times 10^{-2.5}$, and $\text{UV} \times 10^{-5}$. Note that the jumps of the photodissoci-

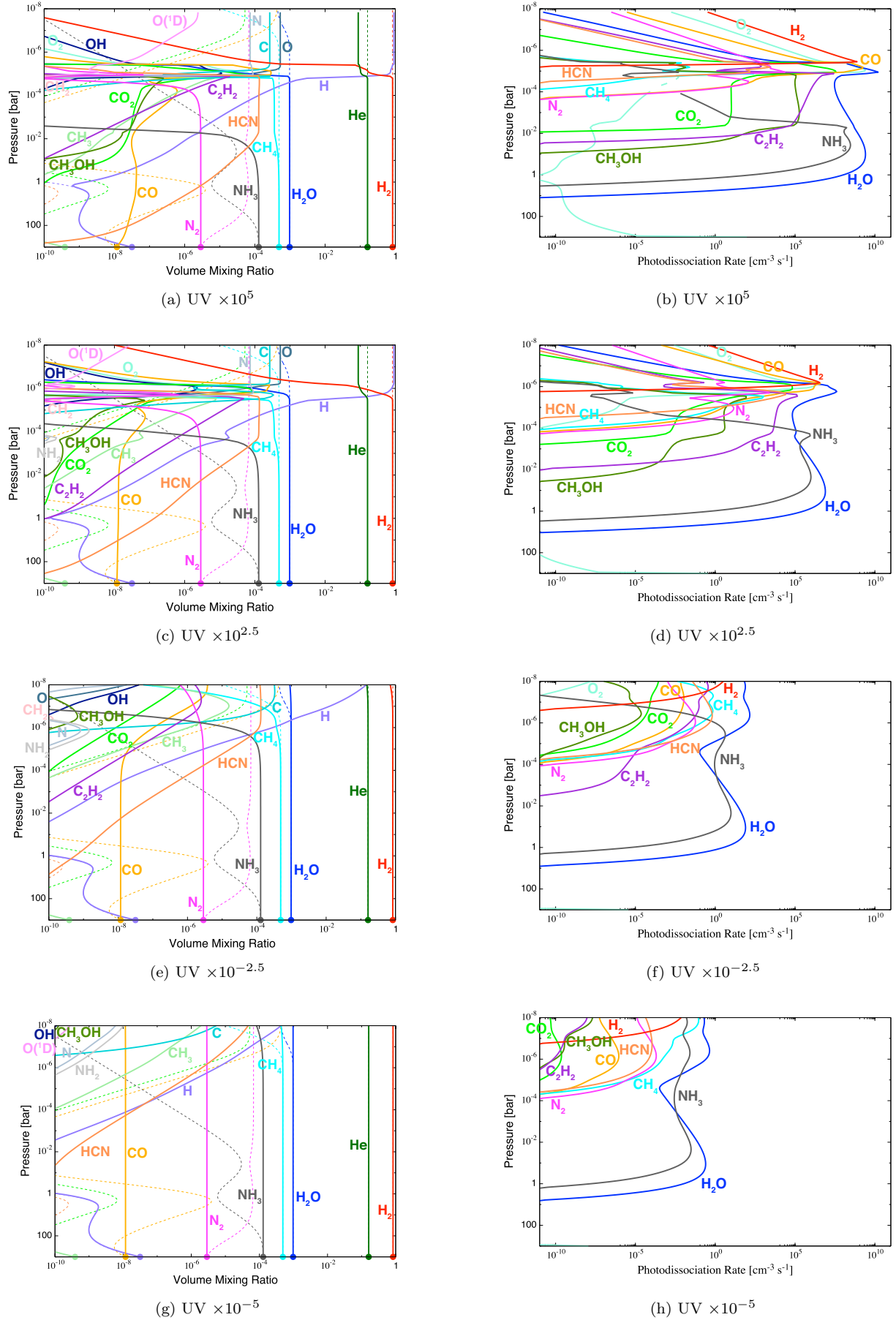


Figure 7. Same as Fig. 3 but for the cases of (a, b) UV $\times 10^5$, (c, d) UV $\times 10^{2.5}$, (e, f) UV $\times 10^{-2.5}$, and (g, h) UV $\times 10^{-5}$.

ation rate of O_2 (light blue) found at $P \sim 10^{-4}$ bar for the case of $\text{UV} \times 10^5$ (b) come from its volume mixing ratio out of our computational precision, so that they are physically meaningless. In the high-UV cases ($\text{UV} \times 10^5$ and $10^{2.5}$), the photodissociation of molecules such as H_2 , H_2O , CH_4 , and NH_3 occurs deeper in the atmosphere than in the fiducial case (Figure 3). This is because photochemistry works more effectively compared to eddy diffusion even at low altitudes because of the intense UV irradiation. Also, the higher the UV irradiation flux, the higher the photodissociation rates themselves. On the other hand, in the low-UV cases ($\text{UV} \times 10^{-2.5}$ and 10^{-5}), only at very high altitudes, photodissociation occurs effectively compared to eddy-diffusion transport, resulting in the constant abundances of molecules such as H_2O , CH_4 , and NH_3 , up to higher altitudes. From Table 1, one finds that the dependence of the photodissociation rates of the haze precursors on the UV irradiation intensity is weaker than linear, namely the higher the UV flux, the smaller proportion of the incoming photons used for the photodissociation of the haze precursors. We have confirmed that this is mainly because larger proportion of the incoming photons are used for the photodissociation of CO and O_2 , which exist at higher altitudes than the hydrocarbons, for higher UV flux.

3.2.2. Particle Growth

Figure 8 also shows the vertical distribution of the haze particles for the four UV irradiation intensities. For higher UV intensities, the mass density and average radii of haze particles are found to be significantly larger because of the higher monomer production rates, nevertheless the particles start to grow at lower altitudes as explained in the previous section. For example, s_{vol} becomes as large as $100 \mu\text{m}$ in the $\text{UV} \times 10^5$ case, while it is only less than $0.1 \mu\text{m}$ in the $\text{UV} \times 10^{-5}$ case at the lower boundary of 10 bar. For the $\text{UV} \times 10^5$ case, because of the high monomer production rate, the disagreement between s_{vol} and s_{surf} is large in the middle atmosphere with the pressure range from $\sim 10^{-5}$ bar to $\sim 10^{-2}$ bar, indicating the broad distribution of the particle size in that region. However, two average radii almost coincide with each other again below the pressure level of $\sim 10^{-2}$ bar because of the decrease in the monomer production rate and the increase in the sedimentation velocity after the transition in gas drag law (from the slip-flow to Stokes-flow regimes), which hampers the particle growth at low altitudes.

3.3. Dependence on Metallicity

Figure 9 shows the transmission spectrum models for the hazy atmosphere with the solar and super-solar

metallicities (colored thick lines). Those without haze are also plotted by thin lines with the same colors.

The main effect of enhanced metallicity is reduction in the scale height of the atmosphere and, thus, in the transit depth for both the clear and hazy atmospheres, as shown in Fig. 9. This makes the effect of haze less pronounced in higher-metallicity cases. Also, haze affects the spectrum only at shorter wavelengths with increasing metallicity. This is because the mass density of the haze particles becomes smaller with increasing metallicity, as seen in § 3.3.2. From an observational point of view, of particular importance are strengths of absorption features (i.e., transit depths relative to baselines). For the clear atmospheres, the strengths are found to decrease with increasing metallicity because of the reduced scale height. On the other hand, in the case of hazy atmospheres, its sensitivity to metallicity is somewhat complicated because both the amount of haze and atmospheric scale height are smaller for higher metallicities. Among the four different metallicity cases, absorption features at shorter wavelengths ($\lesssim 2\text{--}3 \mu\text{m}$) are strongest for the $100\times$ Solar case, while those at longer wavelengths ($\gtrsim 2\text{--}3 \mu\text{m}$), which are less affected by haze, are strongest for the smallest metallicity case of $1\times$ Solar. Note that we discuss investigation of atmospheric metallicity from observations in which we suffer from degeneracy with the reference radius in § 4.1.

3.3.1. Photochemistry and Haze Precursor Production

Figure 10 shows the calculated vertical distributions of the volume mixing ratios (left column) and photodissociation rates (right column) of gaseous species for the $10\times$ Solar, $100\times$ Solar, and $1000\times$ Solar cases (See also Fig. 3 for the solar case).

Apart from simple increases in the fractions of heavy elements, the vertical profile of each species for the metal-rich cases is similar to that for the fiducial case (Fig. 3 (a)). A difference in vertical profile is that H_2O , CH_4 , and NH_3 are lost via photodissociation at slightly lower pressures for higher metallicity atmospheres. This is because the optical depth at a certain pressure is larger for higher metallicity due to the larger abundance of the UV absorbers. This trend can be more clearly seen in the right-column panels of Figure 10.

It is notable that in spite of their increased abundances for higher metallicity, the integrated photodissociation rates of all the haze precursors, CH_4 , HCN , and C_2H_2 , are lower except for that of CH_4 in the $1000\times$ Solar case (see Table 1). This is due to increases of the major photon absorbers, H_2O , CO , CO_2 , and O_2 , existing at higher altitudes than the hydrocarbons, the effect of which is larger than the effect of the decrease in the number

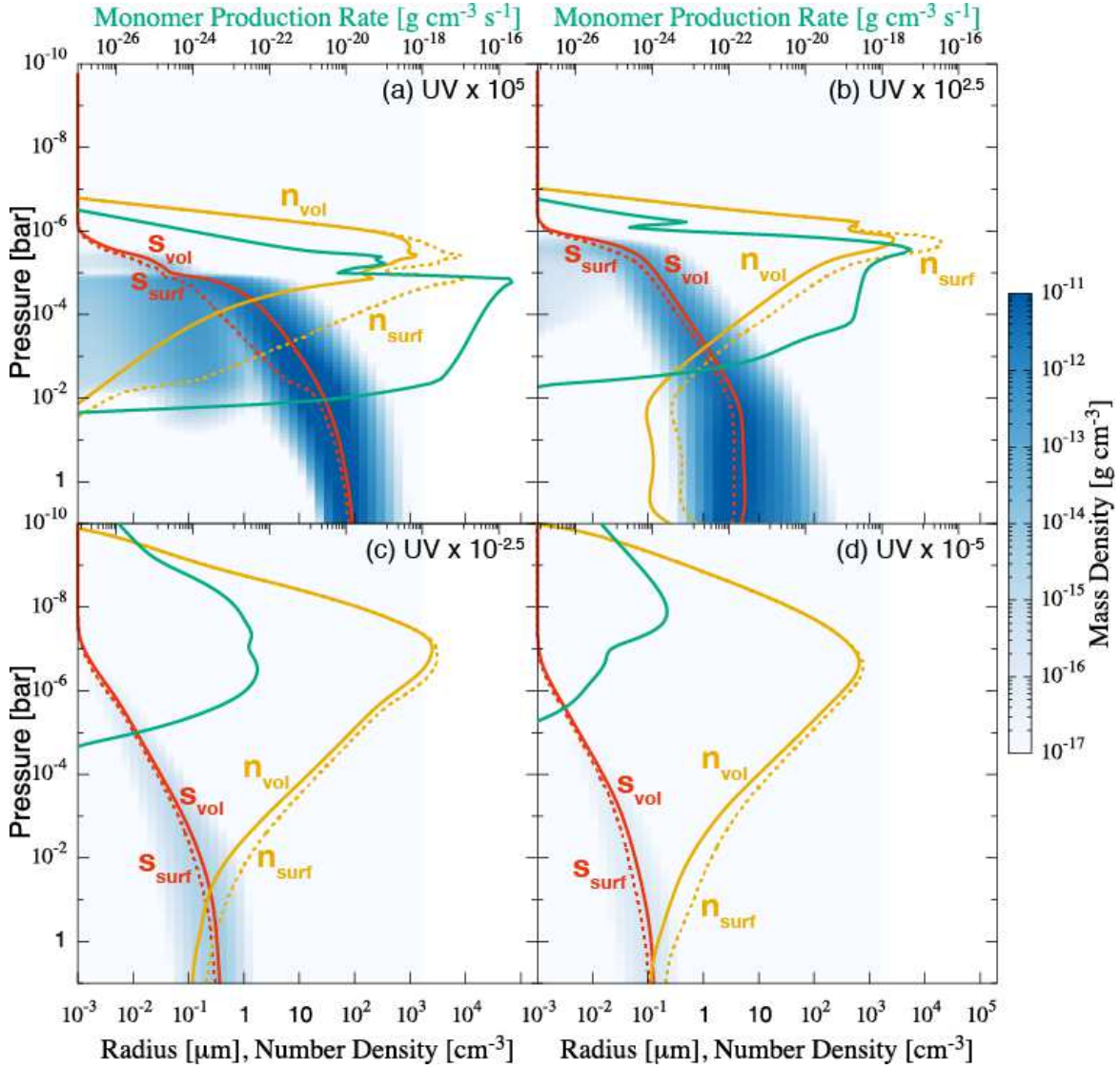


Figure 8. Same as Fig. 4 but for the cases of (a) $UV \times 10^5$, (b) $UV \times 10^{2.5}$, (c) $UV \times 10^{-2.5}$, and (d) $UV \times 10^{-5}$.

of photons absorbed by H_2 . Recent laboratory experiments, however, implied that not only the photodissociation of hydrocarbons, but also that of CO , CO_2 , and H_2O can lead to the formation of haze, implying the existence of multiple formation pathways (Hörst et al. 2018; He et al. 2019). A brief discussion is made in § 4.2.

Compared to the low-metallicity cases, the atmospheric composition for the $1000\times$ Solar case (Fig. 10 (e)) is obviously different: H_2O is the most abundant species over the almost entire region. Among the carbon-bearing species, CO_2 is the most abundant rather than CH_4 and the abundance of C_2H_2 is small because of the high O/H ratio of 0.5812. From Figure 10 (d) and (f), it is found that the photodissociation rate of CH_4 is higher due to its larger abundance in the $1000\times$ Solar case than in the $100\times$ Solar case, while that of C_2H_2 is smaller due to its smaller abundance in the former case than in the

latter. In total, the total photodissociation rates of haze precursors for the $100\times$ Solar and $1000\times$ Solar cases are almost similar (see Table 1).

3.3.2. Particle Growth

Figure 11 shows the vertical distribution of haze particles for such three super-solar metallicities. Both the mass density and average radii of the haze particles in the lower atmosphere are found to be smaller for higher metallicities (see also Fig. 4 for the $1\times$ Solar metallicity). This is partly because the integrated monomer production rate is smaller for the higher metallicity atmosphere, as described in the last subsection. Also, the particles settle down from the upper to lower boundary on a shorter timescale for the higher metallicity atmosphere. This is because the pressure scale height H becomes small with the atmospheric mean molecular

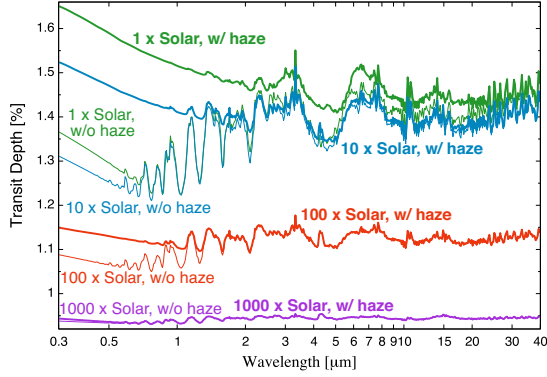


Figure 9. Transmission spectrum models for four different atmospheric metallicities, solar (green, same as the green line in Fig. 5; "1 \times Solar") and 10 times (blue; "10 \times Solar"), 100 times (red; "100 \times Solar"), and 1000 times (purple; "1000 \times Solar") higher than the solar. The thick and thin lines represent the spectra of the haze-covered and haze-free atmospheres, respectively. Note that the transmission spectrum models are smoothed for clarity.

weight μ more greatly than the particle sedimentation velocity v_{sed} does (i.e., $H \propto \mu^{-1}$, while $v_{\text{sed}} \propto \mu^{-1/2}$; see Eq. (13) of Paper I). Thus, in the higher metallicity cases, there is less time for the particles to grow before reaching the lower boundary. This effect can be seen clearly by comparison between the 100 \times Solar and 1000 \times Solar metallicity cases. Although the integrated monomer production rates are comparable to each other, the mass density and averaged radii of the haze particles are smaller in the 1000 \times Solar case.

3.4. Dependence on C/O ratio

Figure 12 shows the transmission spectrum models for the atmosphere with haze for four different values of C/O = 0.5 (green), 1 (orange), 10 (red), and 1000 (purple). The transmission spectrum for the haze-free atmosphere for C/O = 0.5 is also plotted (black line). Here we consider large values of C/O, because the effect of hydrocarbon haze on transmission spectra is of special interest in this study.

The transit depth increases with increasing C/O at each wavelength. This is simply because larger amounts of haze are produced for higher values of C/O (see § 3.4.2). In particular, in the case of C/O = 1000, almost all the molecular absorption features are hidden by the abundant haze and, instead, the absorption features of the haze particles still remain at 3.0, 4.6, and 6.3 μm . We have confirmed that even in the extreme case of C/O = 10^{10} , the spectrum for the atmosphere with haze shows such haze features and never becomes flat, because the total photodissociation rates of hydro-

carbons are limited not by the amount of carbon, but by the incoming photon flux.

3.4.1. Photochemistry and Haze Precursor Production

Figure 13 shows the calculated vertical distributions of volume mixing ratios (left column) and photodissociation rates (right column) of gaseous species for C/O = 1, 10, and 1000. In the case of C/O = 1, the abundance of CH_4 is almost equal to that of H_2O in the lower atmosphere ($P \gtrsim 10^{-4}$ bar), because almost all of the C and O are in the form of CH_4 and H_2O , respectively. As can be expected, the abundances of oxygen-bearing species such as H_2O , O, CO, CO_2 , OH, O_2 , and CH_3OH decrease with increasing C/O, while the other trends are similar to those in the fiducial case (C/O = 0.5; Fig. 3 (a)).

The integrated photodissociation rates of the haze precursors, CH_4 , HCN, and C_2H_2 , become higher with increasing C/O ratio, except for CH_4 and HCN for C/O = 1000 (see Table 1). This is due to two effects: One is the increased abundances of those haze precursors, and another is the decreased abundances of H_2O and CO, which are the major photon absorbers in the fiducial case. Note that the integrated photodissociation rates of CH_4 and HCN for C/O = 1000 becomes smaller than those for C/O = 10, because C_2H_2 existing at higher altitudes absorbs more photons and inhibits them from absorbing the photons. Thus, the sum of the integrated photodissociation rates of the three haze precursors is higher for higher values of C/O. Also, the photodissociation region of the three haze precursors becomes broader for higher C/O. This is because the atmosphere becomes less optically-thick due to the decrease of the major photon absorbers such as CO and H_2O .

3.4.2. Particle Growth

Figure 14 shows the vertical distribution of the haze particles for such three different values of C/O. As explained in § 3.4.1, the integrated monomer production rate is higher for higher C/O. As a result, both the mass density and average radii of the haze particles in the lower atmosphere are found to be larger for higher C/O (see also Fig. 4 for C/O = 0.5), which has a significant effect on the transit depths (see Fig. 12). Also, the sizes of the haze particles are more diverse for higher C/O because of the broader monomer production region.

3.5. Dependence on Eddy Diffusion Coefficient

Figure 15 shows the transmission spectrum models for the atmosphere with haze for three different values of the eddy diffusion coefficient, K_{zz} , 1×10^9 (light blue; high- K_{zz}), 1×10^7 (green; fiducial), and $1 \times 10^5 \text{ cm}^2 \text{ s}^{-1}$

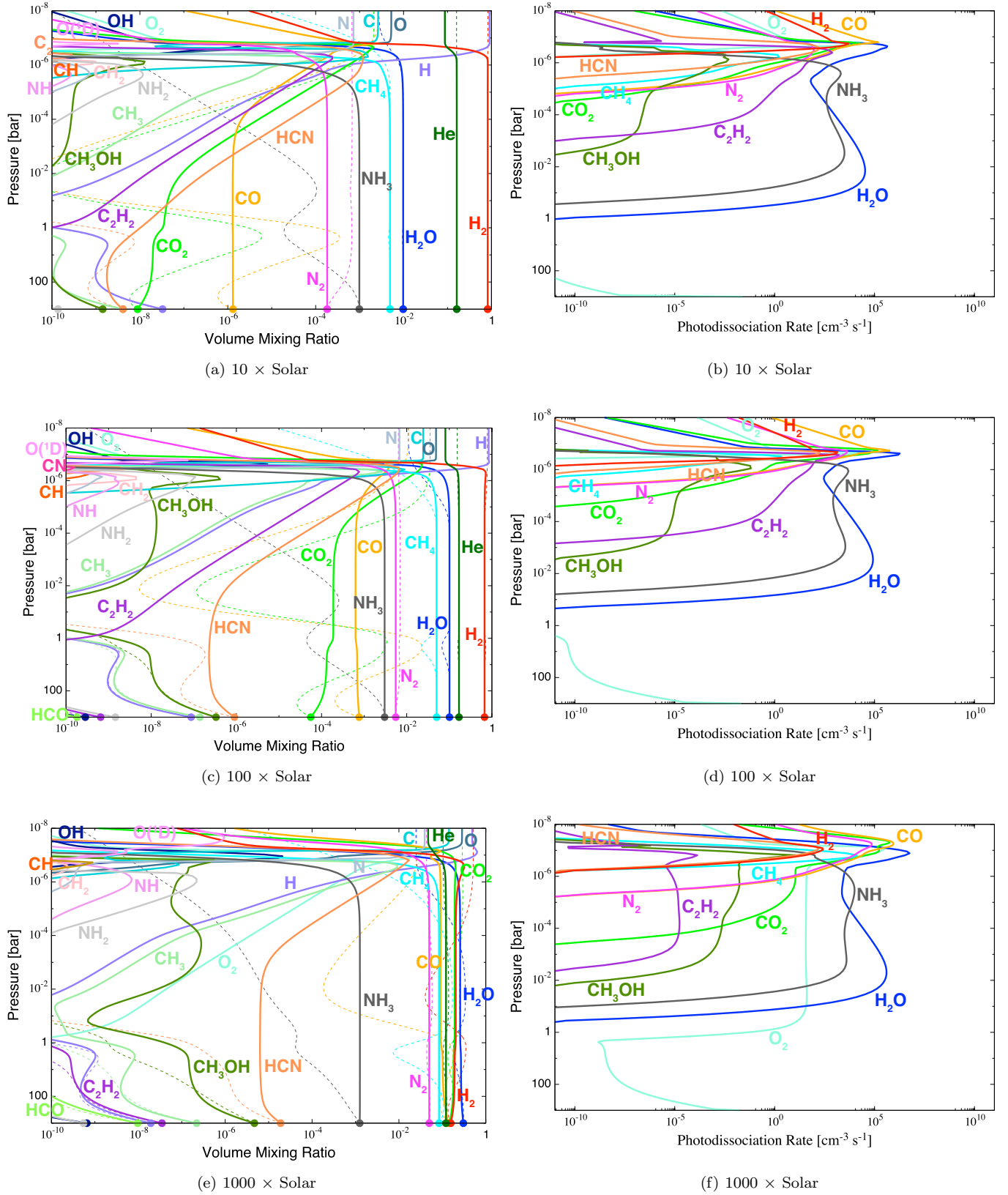


Figure 10. Same as Fig. 3 but for the cases of (a, b) $10 \times \text{Solar}$, (c, d) $100 \times \text{Solar}$, and (e, f) $1000 \times \text{Solar}$ metallicity atmospheres.

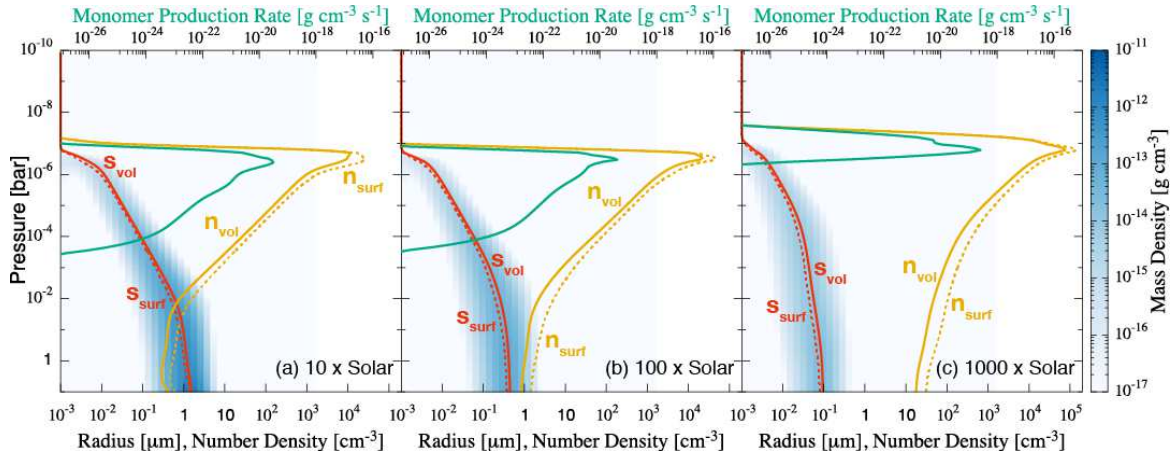


Figure 11. Same as Fig. 4 but for the cases of (a) $10 \times$ Solar, (b) $100 \times$ Solar, and (c) $1000 \times$ Solar metallicity atmospheres.

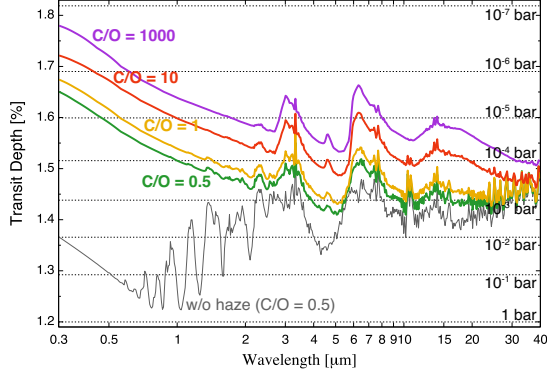


Figure 12. Transmission spectrum models for the atmosphere with haze for the four different cases where $C/O = 0.5$ (green line, same as the green line in Fig. 5), 1 (orange line), 10 (red line), and 1000 (purple line). The transmission spectrum for the atmosphere without haze for the case of $C/O = 0.5$ is also plotted (black line, same as the black line in Fig. 5). As in Fig. 5, horizontal dotted lines represent the transit depths corresponding to the pressure levels from 1×10^{-7} bar to 1 bar for the atmosphere in the case of $C/O = 0.5$. Note that the transmission spectrum models are smoothed for clarity.

(purple; low- K_{zz}). The green and gray lines are the fiducial models with and without haze, respectively, shown in Fig. 5.

In the high- K_{zz} model, one finds a steep Rayleigh-scattering slope in the optical and more prominent molecular-absorption features in the infrared, relative to the fiducial and low- K_{zz} models. As explained in detail in § 3.5.2, this is because efficient eddy diffusion removes haze particles from the upper atmosphere, making the atmosphere optically thinner.

The low- K_{zz} model is almost the same as the fiducial one. This is due to similar distributions of haze particles (also see § 3.5.2). Slight differences in absorption feature are found at 11 and 14 μm . The former is due to a different distribution of NH_3 , while the latter due to that of $\text{NH}_3 + \text{HCN}$, as shown in § 3.5.1.

3.5.1. Photochemistry and Haze Precursor Production

Figure 16 (a) and (c) show the calculated vertical distributions of gaseous species for $K_{zz} = 1 \times 10^9$ and $1 \times 10^5 \text{ cm}^2 \text{ s}^{-1}$, respectively (also see Fig. 3 for $K_{zz} = 1 \times 10^7 \text{ cm}^2 \text{ s}^{-1}$). As found in each panel, below a certain pressure (or above an altitude), the volume mixing ratios of H_2O , CH_4 , and NH_3 are found to deviate from the constant values, which are almost equal to those at the lower boundary. Such a threshold pressure (or altitude) decreases (or increases) with increasing K_{zz} , because the transport by eddy diffusion occurs more efficiently to compensate for the loss of those molecules via photodissociation for the higher value of

K_{zz} . As for NH_3 , such an effect appears as its 11 μm absorption feature in the transmission spectrum, as described above (see Fig. 15). By contrast, photochemical products such as C_2H_2 become more abundant, as K_{zz} decreases, because photochemistry dominates over the transport of thermochemical products.

The distribution of HCN, which contributes to the 14 μm feature in Fig. 15, depends on eddy diffusion coefficient in a somewhat complicated way. As seen in Figure 16 (a) and (c), the higher the value of K_{zz} , the higher the altitude above which HCN outnumbers NH_3 as the dominant nitrogen-bearing species. Also, HCN remains as the dominant nitrogen-bearing species against N up to higher altitudes for higher values of K_{zz} . This is because the efficient eddy diffusion transport prevents N atoms from being produced by photodissociation of HCN. In short, the region where HCN exists as the dominant nitrogen-bearing species is the narrowest in the fiducial case among the three cases. This is one of the effects responsible for the stronger absorption feature at 14 μm in the low- K_{zz} model than in the fiducial case. In the low- K_{zz} model, in addition to NH_3 , HCN also contributes to the absorption feature. To be exact, the existence of HCN in the broader pressure range compensates for the loss of NH_3 from the lower altitude and, thus, results in the increase of absorption feature at 14 μm in the low- K_{zz} model. In the high- K_{zz} model, the 14 μm feature is almost the same as that in the haze-free model with the fiducial value of K_{zz} because the haze abundance is small and also, HCN exists only at quite high altitudes, so that it has negligible contribution to the feature in this case.

Figure 16 (b) and (d) plot the vertical profile of the photodissociation rate of each species for such two values of K_{zz} . In higher- K_{zz} cases, photodissociation occurs at lower pressures (higher altitudes) because molecules are transported up to lower pressures (higher altitudes) for higher values of K_{zz} . As for haze precursors, the integrated photodissociation rates of CH_4 and HCN are higher for higher values of K_{zz} , because they are lifted up to higher altitudes by the efficient transport (see Table 1). By contrast, the integrated photodissociation rate of C_2H_2 becomes smaller, as K_{zz} becomes large. This is because of its lower abundance for the higher value of K_{zz} . Thus, in contrast to the fiducial and low- K_{zz} cases, in the high- K_{zz} case, C_2H_2 is the last precursors to photodissociate among the three. Putting all those effects together, the sum of the photodissociation rate of the three haze precursors is lower for higher values of K_{zz} .

3.5.2. Particle Growth

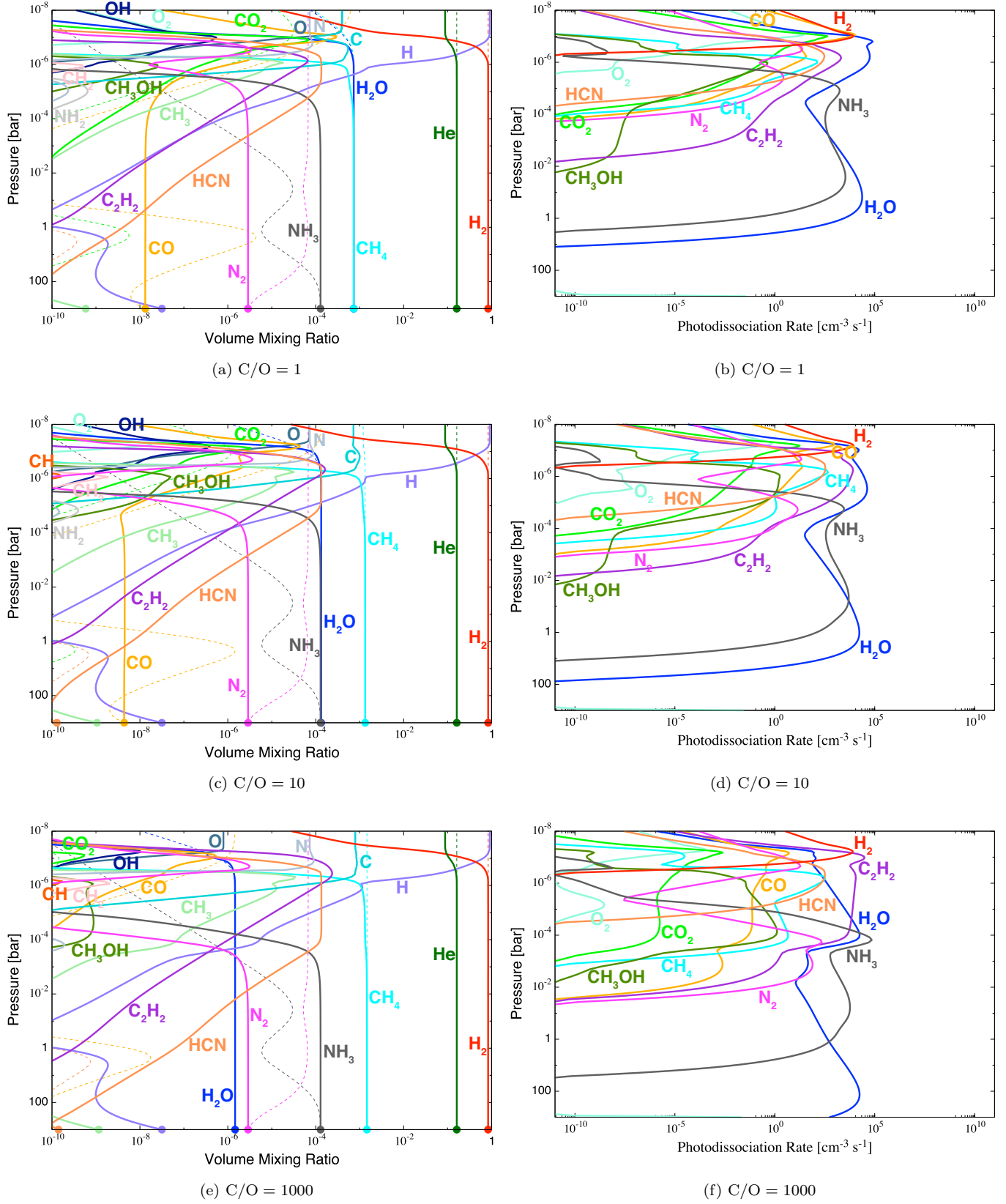


Figure 13. Same as Fig. 3 but for the cases of the atmospheres with C/O = (a, b) 1, (c, d) 10, and (e, f) 1000.

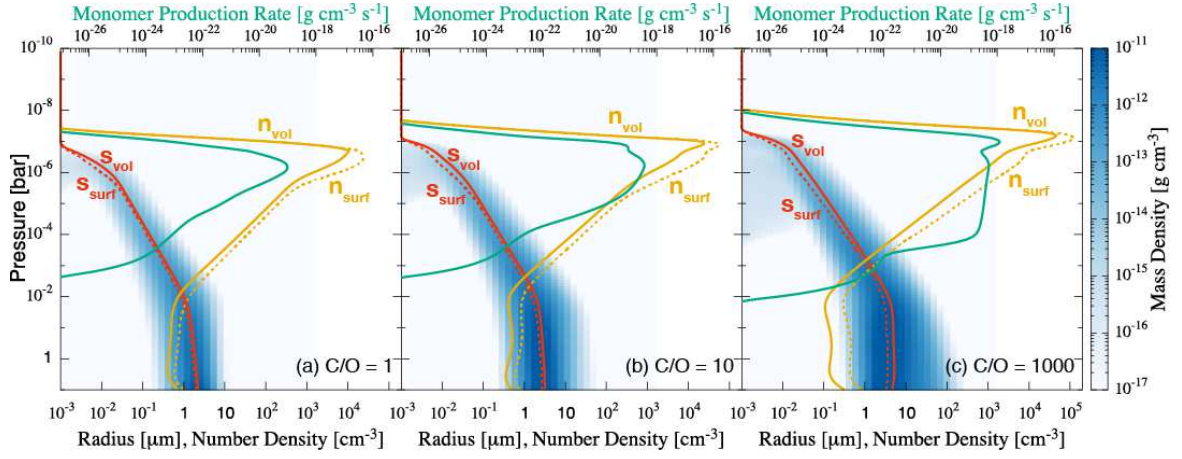


Figure 14. Same as Fig. 4 but for the cases of atmospheres with $\text{C/O} =$ (a) 1, (b) 10, and (c) 1000.

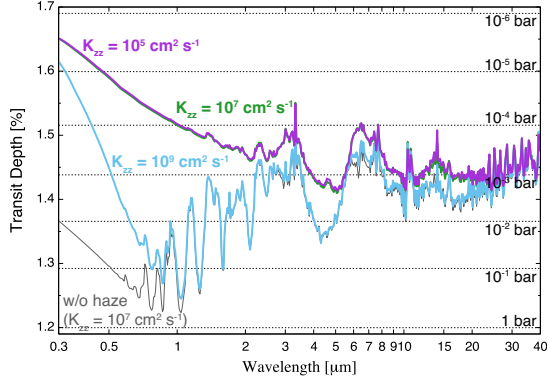


Figure 15. Transmission spectrum models for the atmosphere with haze for the three different cases where $K_{zz} = 1 \times 10^9 \text{ cm}^2 \text{ s}^{-1}$ (light-blue line), $K_{zz} = 1 \times 10^7 \text{ cm}^2 \text{ s}^{-1}$ (green line, same as the green line in Fig. 5), and $K_{zz} = 1 \times 10^5 \text{ cm}^2 \text{ s}^{-1}$ (purple line). The transmission spectrum for the atmosphere without haze for the case of $K_{zz} = 1 \times 10^7 \text{ cm}^2 \text{ s}^{-1}$ is also plotted (black line, same as the black line in Fig. 5). As in Fig. 5, horizontal dotted lines represent the transit depths corresponding to the pressure levels from 1×10^{-6} bar to 1 bar for the atmosphere in the case of $K_{zz} = 1 \times 10^7 \text{ cm}^2 \text{ s}^{-1}$. Note that the transmission spectrum models are smoothed for clarity.

Figure 17 shows the vertical profiles of the haze particles for $K_{zz} =$ (a) 1×10^9 and (b) $1 \times 10^5 \text{ cm}^2 \text{ s}^{-1}$. First, the particles are found to grow only to $0.1 \mu\text{m}$ in the high- K_{zz} case in contrast to the fiducial and low- K_{zz} cases where the particles grow to $\gtrsim 1 \mu\text{m}$. This is because over the almost entire region the eddy diffusion with such high K_{zz} brings about descent of the particles and its velocity is higher than the sedimentation velocity, resulting in a rapid downward transport of the particles. Such an effect is negligible in the fiducial and low- K_{zz} cases. This is why the haze particles hardly obscure molecular features in the infrared transmission spectrum in the high- K_{zz} case (see Fig. 15). Instead, in the high- K_{zz} case, such small haze particles ($\lesssim 0.1 \mu\text{m}$), which exist even in the lower atmosphere, produce the steep Rayleigh-scattering slope in the optical. Note that the slightly low integrated monomer production rate for the high- K_{zz} also inhibits particle growth. We have, however, confirmed that such a slightly low production rate has a minor effect, but the efficient eddy diffusion is responsible for the prohibition of the particle growth in the high- K_{zz} case.

The distribution of haze particles for the low- K_{zz} is almost similar to that for the fiducial case (see Fig. 4). This is because eddy-diffusive mixing hardly contributes to the particle transport and the monomer production rates are almost similar in both cases. Thus, the trans-

mission spectra are also similar in both cases, as shown in Fig. 15.

3.6. Dependence on Temperature

Figure 18 shows the transmission spectrum models for the higher irradiation temperature T_{irr} of 1290 K (red), which are compared with the fiducial models with $T_{\text{irr}} = 790$ K (green). Regardless of haze, the transit depths are larger and the spectral features are more pronounced for the higher- T_{irr} atmosphere, because of larger atmospheric scale height. Comparing the spectra with (thick line) and without (thin line) haze for each temperature case, one finds that the presence of the haze has a smaller effect on the spectrum in the higher- T_{irr} case when taking the scale-height difference into account. This is because of the smaller mass density of the haze particles, as explained below.

In Figure 19, we show (a) the calculated vertical distributions and (b) photodissociation rate profiles of gaseous species for $T_{\text{irr}} = 1290$ K. Unlike in the fiducial case with $T_{\text{irr}} = 790$ K (Fig. 3 (a)), not CH_4 but CO is the dominant carbon-bearing species and is equal in abundance to H_2O in the middle atmosphere (10^{-4} bar $\lesssim P \lesssim 10$ bar), because CO is more thermodynamically stable than CH_4 at high temperatures. Therefore, the photodissociation rate of CO is also larger than in the fiducial case. Likewise, N_2 , H , and CO_2 are more abundant than in the fiducial case because of stability at high temperatures, while CH_4 and NH_3 are less abundant.

The haze precursors are all less abundant in the photodissociation region ($P \sim 10^{-6}$ bar) because carbon exists in the form of CO over the almost entire region. HCN also exists even in the lower atmosphere unlike in the fiducial case, where it is thermochemically produced due to the high temperatures. The integrated photodissociation rates of CH_4 , HCN , and C_2H_2 are all smaller compared to those in the fiducial case because of their decreased abundances (see Table 1).

Figure 20 shows the vertical distribution of the haze particles for $T_{\text{irr}} = 1290$ K. The total mass density of the haze particles is found to be slightly smaller, because as seen above, the sum of the integrated photodissociation rates of haze precursors is smaller and, thus, the assumed monomer production rate is smaller than in the fiducial case.

4. DISCUSSIONS

4.1. Implications for Observations

In this paper, over broad ranges of poorly-constrained parameters, we have explored which combinations of those parameters result in larger or smaller absorption features in transmission spectra of warm super-Earth at-

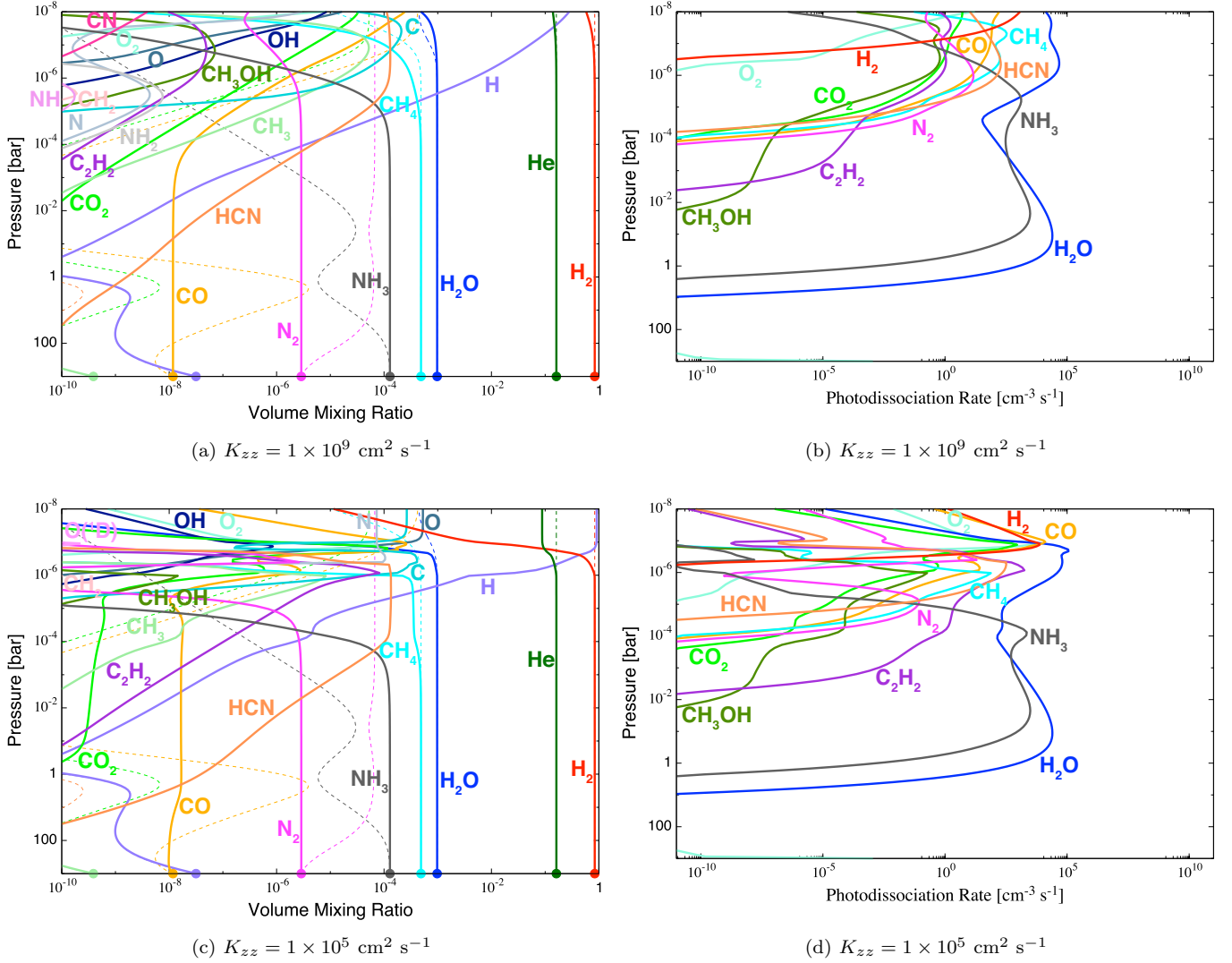


Figure 16. Same as Fig. 3, but for two different values of eddy diffusion coefficient, K_{zz} : (a, b) $K_{zz} = 1 \times 10^9 \text{ cm}^2 \text{ s}^{-1}$ and (c, d) $K_{zz} = 1 \times 10^5 \text{ cm}^2 \text{ s}^{-1}$.

mospheres with hydrocarbon haze. We have found that atmospheres with lower UV irradiation, lower C/O ratio, higher eddy diffusion coefficient, and higher temperature result in more pronounced molecular-absorption features compared to the fiducial case. We have also found that transmission spectra depend on metallicity in a somewhat complicated way: At relatively short wavelengths ($\lesssim 2\text{--}3 \mu\text{m}$), moderate metallicities (such as 100 times the solar metallicity) result in strong absorption features, because the effects of low monomer production rate and small scale height compete with each other for high metallicities; At relatively long wavelengths ($\gtrsim 2\text{--}3 \mu\text{m}$), where haze has a small effect on transmission spectra, lower metallicities result in more pronounced features.

The idea that warm exoplanets have atmospheres covered with hydrocarbon haze seems to be consistent with an observationally suggested correlation between transmission spectra and atmospheric temperatures. In § 3.6, we have demonstrated that the higher the temperature, the smaller the photodissociation rates of the hydrocarbon precursors and the production rates of haze monomers are. That is because CO rather than CH_4 becomes the dominant carbon-bearing species at high temperatures. Thus, the resultant spectra for higher atmospheric temperatures show more distinct molecular absorption features. This is consistent with the reported observational trend such that stronger absorption features are seen in transmission spectra of hotter planets, although other planetary properties may affect such a correlation (Stevenson 2016; Heng 2016;

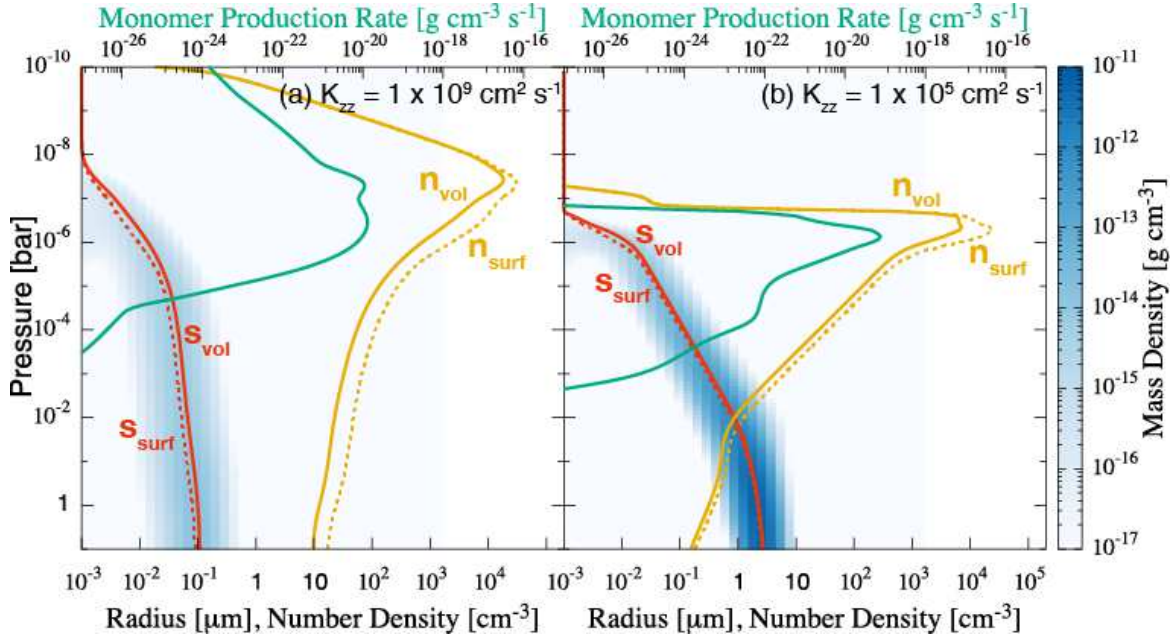


Figure 17. Same as Fig. 4, but for two different values of eddy diffusion coefficient, K_{zz} : (a) $K_{zz} = 1 \times 10^9 \text{ cm}^2 \text{ s}^{-1}$ and (b) $K_{zz} = 1 \times 10^5 \text{ cm}^2 \text{ s}^{-1}$.

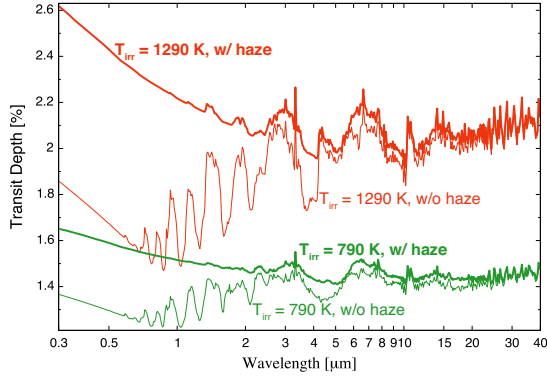


Figure 18. Transmission spectrum models for the atmospheres with haze for the cases of $T_{\text{irr}} = 1290 \text{ K}$ (red thick line) and $T_{\text{irr}} = 790 \text{ K}$ (green thick line, same as the green line in Fig. 5). The transmission spectrum for the atmosphere without haze for the cases of $T_{\text{irr}} = 1290 \text{ K}$ (red thin line) and $T_{\text{irr}} = 790 \text{ K}$ (green thin line, same as the black line in Fig. 5) are also plotted. Note that the transmission spectrum models are smoothed for clarity.

Crossfield & Kreidberg 2017). However, recent laboratory experiments implied that CH_4 is not necessarily required for the haze formation, and instead, CO and CO_2 can provide an alternative source of carbon (Hörst et al. 2018; He et al. 2019). A brief discussion on this is made in § 4.2.

Next, we explore observational strategies for constraining the composition of hazy atmospheres. In Figure 21, we plot the calculated differences in band-integrated transit depths between several photomet-

ric bands and the J band as a function of metallicity for two different values of the eddy diffusion coefficient, K_{zz} , (a) 1×10^7 and (b) $1 \times 10^9 \text{ cm}^2 \text{ s}^{-1}$. The values of the transit depths are normalized by $\Delta D_{H,\text{fiducial}} = 2R_{\text{ref}}H_{\text{ref}}/R_s^2$, which is the transit depth difference caused by one atmospheric scale height for $H_{\text{ref}} \ll R_{\text{ref}}$ (Brown 2001) in the fiducial case ($1 \times \text{Solar}$ and $K_{zz} = 1 \times 10^7 \text{ cm}^2 \text{ s}^{-1}$). Here, R_{ref} is the planetocentric radius at a reference pressure, for which we assume $1 \times 10^{-3} \text{ bar}$, H_{ref} is an atmospheric scale height at R_{ref} , and R_s is the stellar radius. We adopt the value of $\Delta D_{H,\text{fiducial}}$ in all the cases of the different metallicities and K_{zz} . The values of the effective wavelength λ_{eff} and the band width $\Delta\lambda$ we adopt for each band are listed in Table 2, which we take from Table 2.1 of Binney & Merrifield (1998).

As shown in Figure 21, the absolute value of the difference in transit depth between each band and the J band generally decreases with increasing metallicity for both the hazy (solid lines) and haze-free (dotted lines) atmospheres because atmospheric scale height decreases. It is demonstrated that simultaneous observations at shorter wavelengths are more suitable for constraining atmospheric metallicity, because of the larger dependence of the transit depth difference on metallicity. This is due to the Rayleigh-scattering slope produced by haze particles.

For the high- K_{zz} case (panel b), the transit depth differences for two shortest wavelength bands (U and B) are larger than those for the fiducial K_{zz} case due to the

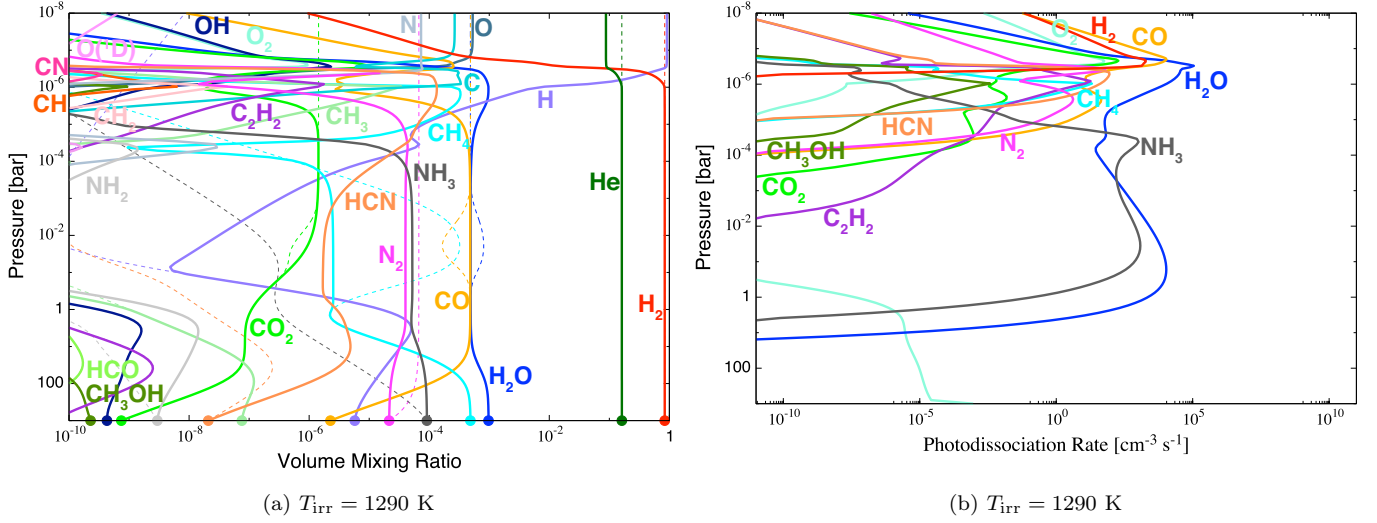


Figure 19. Same as Fig. 3 but for the cases of the irradiation temperature of $T_{\text{irr}} = 1290 \text{ K}$.

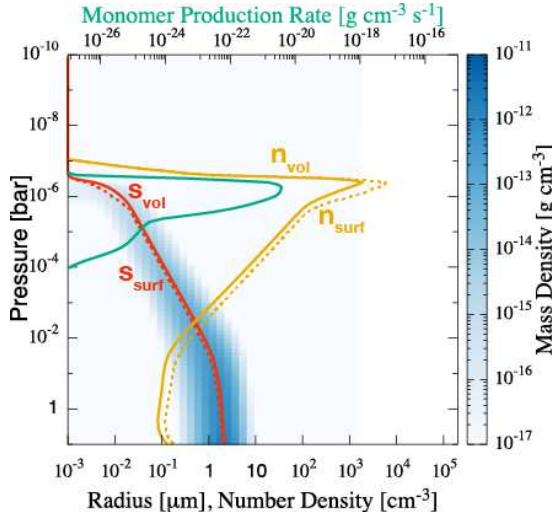


Figure 20. Same as Fig. 4 but for the case of $T_{\text{irr}} = 1290 \text{ K}$.

efficient downward transport of haze particles (§ 3.5). Also, because of the small monomer production rate, the transit depth differences for long wavelength bands (H , K , L , and M) for the hazy atmospheres almost coincide with those for the haze-free atmospheres.

From these two figures, one finds that in some cases, from broad-band observations alone, we suffer from a degeneracy between metallicity and eddy diffusion coefficient. For example, the transit depth difference of U - J (purple line) for $1 \times$ Solar metallicity atmosphere with the fiducial K_{zz} value (a) is almost the same as that for $10 \times$ Solar metallicity atmosphere with the high K_{zz} value (b). Certainly such broad-band observations especially in the optical are useful for target selection aiming for detailed space-based observations in the sense that

Table 2. Band

Band	λ_{eff} [nm]	$\Delta\lambda$ [nm]
U	365	66
B	445	94
V	551	88
R	658	138
I	806	149
J	1220	213
H	1630	307
K	2190	390
L	3450	472
M	4750	460

NOTE—Values of the effective wavelength λ_{eff} and the band width $\Delta\lambda$ we adopt for each band, which is taken from Table 2.1 of Binney & Merrifield (1998).

atmospheres showing steep spectral scopes in the optical are likely to show strong absorption features in the infrared. However, for obtaining precise constraints on metallicity, it is necessary to measure the strength of absorption features in the infrared, where the contribution of haze is small.

Recent observational precisions are already high enough to distinguish transit depth differences smaller than one atmospheric scale height for some super-Earths such as for GJ 1214b and HAT-P-11b even with ground-based telescopes such as the Okayama 188cm one

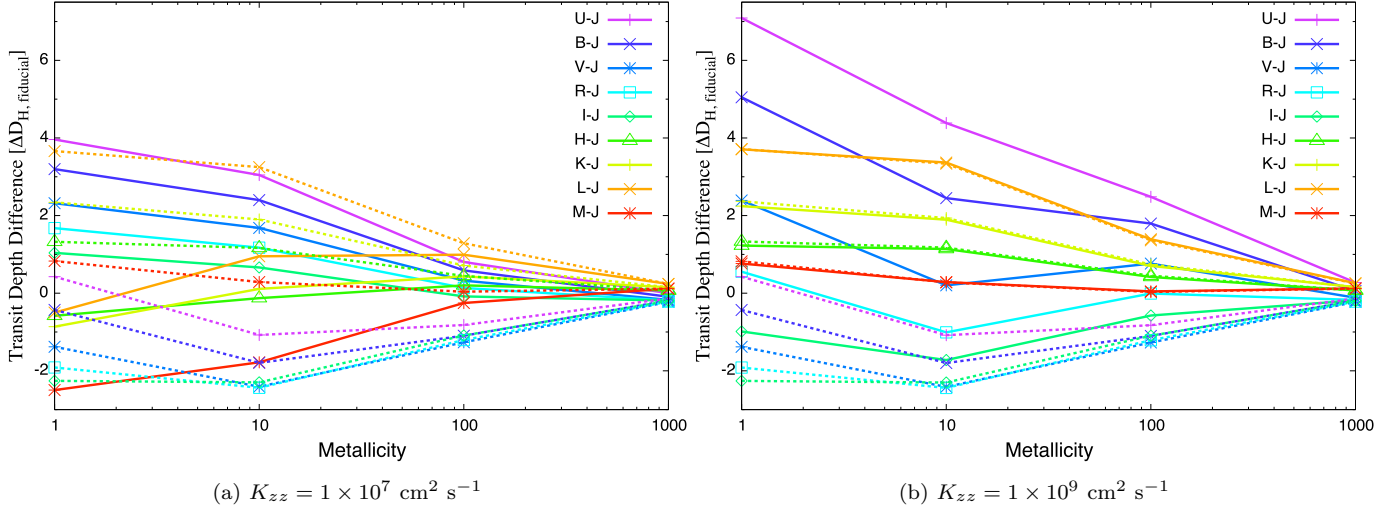


Figure 21. Differences of the band-integrated transit depths from that in the J band as a function of atmospheric metallicity for two different values of the eddy diffusion coefficient, K_{zz} , (a) 1×10^7 and (b) 1×10^9 $\text{cm}^2 \text{s}^{-1}$. Transit depths for the hazy atmospheres are plotted with solid lines, while those for the haze-free atmospheres are plotted with dashed lines. The values of the transit depths are normalized by the transit depth difference caused by one atmospheric scale height in the fiducial case ($1 \times \text{Solar}$ and $K_{zz} = 1 \times 10^7$ $\text{cm}^2 \text{s}^{-1}$), $\Delta D_{H, \text{fiducial}} = 2R_{\text{ref}}H_{\text{ref}}/R_s^2$, where R_{ref} is the planetocentric distance to a reference pressure level, H_{ref} is the pressure scale height at R_{ref} and R_s is the stellar radius (see text for the details).

equipped with the Multicolor Simultaneous Camera for studying Atmospheres of Transiting exoplanets (MuSCAT) (Narita et al. 2015; Fukui et al. 2016). Although being still limited due to lack of bright targets, the number of such exoplanets is expected to greatly increase, thanks to the Transiting Exoplanet Survey Satellite (TESS; Ricker et al. 2014) launched in April 2018 and PLANetary Transits and Oscillations of stars (PLATO; Rauer et al. 2014) to be launched in 2026. Also, the James Webb Space Telescope (JWST; Gardner et al. 2006) to be launched in 2021 and Atmospheric Remote-sensing Exoplanet Large-survey (ARIEL; Tinetti et al. 2018) to be launched in 2028 will enable us to precisely measure the strength of absorption features at longer wavelengths, where the contribution of haze is small. These facts indicate the possibility of obtaining constraints as to atmospheric properties such as metallicity for a number of exoplanets.

4.2. Implications from Experiments

A series of experiments have been recently conducted to measure the production rate of hydrocarbon haze, simulating the environments of warm, high-metallicity exoplanet atmospheres in a chamber (He et al. 2018a; Hörst et al. 2018; He et al. 2018b). For the two enriched gases, $100 \times \text{Solar}$ and $1000 \times \text{Solar}$, with temperature of 400 K, the measured production rates are 0.25 and 10.00 mg h^{-1} , respectively (cf. 7.4 mg h^{-1} for the simulated Titan’s atmosphere), indicating that the efficiency of photo-dissociative conversion from hydrocar-

bons to haze particles becomes higher with metallicity. However, we have to keep in mind that results obtained in a chamber cannot be applied directly to the real atmosphere because photochemistry in atmospheres is controlled not only by local conditions unlike in chamber experiments. We must take into account the extinction of photo-dissociating radiation through the atmosphere from the host star to the altitude of interest. Indeed, as we have shown in § 3.3, the higher the atmospheric metallicity is, the lower the photodissociation rates of the low-order hydrocarbons such as CH_4 , HCN , and C_2H_2 are basically (see Table 1), since a rise in atmospheric metallicity leads to increases of H_2O , CO , CO_2 , and O_2 exiting at higher altitudes than the hydrocarbons and those molecules absorb more photons, hampering the photodissociation of the hydrocarbons.

In this section, using the data of haze production rate from the above experiments, we explore the transmission spectra for the $100 \times \text{Solar}$ and $1000 \times \text{Solar}$ atmospheres. Unlike the assumption we have used so far in this paper, here we define the integrated monomer production rate throughout the atmosphere, \dot{M}_{exp} , as

$$\dot{M}_{\text{exp}} = \beta \frac{I_{\text{Ly}\alpha}}{I_{\text{Ly}\alpha, \text{Titan}}} \dot{M}_{\text{Titan}}, \quad (4)$$

where β is a tuning parameter described below, $I_{\text{Ly}\alpha}$ is the incident stellar Ly α flux at the planet’s orbital distance, and $I_{\text{Ly}\alpha, \text{Titan}}$ and \dot{M}_{Titan} are the incident solar Ly α flux and integrated monomer production rate in the atmosphere of Titan, respectively. Note that this is

the same equation as Eq. (35) of Paper I. Namely, we assume that the integrated production rate is proportional to the incident stellar Ly α flux like in Paper I. Note that although we have found that the dependence of the photodissociation rates of the haze precursors on the UV irradiation intensity is weaker than the linear-relationship in § 3.2, we adopt this assumption for simplicity. We adopt the parameter β as the ratio of the experimental production rates of the 100×Solar and 1000×Solar gas to that for the simulated Titan’s atmosphere, namely, $0.25/7.4 = 0.034$ and $10.00/7.4 = 1.4$, respectively. For the value of \dot{M}_{Titan} , we adopt $1 \times 10^{-14} \text{ g cm}^{-2} \text{ s}^{-1}$ since microphysical models, photochemical models, and laboratory simulations all imply that the production rate of the monomers on Titan is in the range between 0.5×10^{-14} and $2 \times 10^{-14} \text{ g cm}^{-2} \text{ s}^{-1}$ (McKay et al. 2001). Also, we use $6.2 \times 10^9 \text{ photons cm}^{-2} \text{ s}^{-1}$ for $I_{\text{Ly}\alpha, \text{Titan}}$ (Trainer et al. 2006) and $3.3 \times 10^{13} \text{ photons cm}^{-2} \text{ s}^{-1}$ for $I_{\text{Ly}\alpha}$ using the values of the observed Ly α flux of GJ 1214 (Youngblood et al. 2016) and GJ 1214b’s semi-major axis (Anglada-Escudé et al. 2013).

We assume that the monomer production rate is proportional to the sum of the photodissociation rates of CH₄, HCN, and C₂H₂ and define the modified monomer production rate at each altitude, $p_{\text{exp}}(v_1, z)$, as

$$p_{\text{exp}}(v_1, z) = \frac{\dot{M}_{\text{exp}}}{\dot{M}} p(v_1, z), \quad (5)$$

where \dot{M} is the integrated production rate throughout the atmosphere, which we have adopted in the previous part and is given by

$$\dot{M} = \int_0^\infty p(v_1, z) dz. \quad (6)$$

From Eq. (4), the values of \dot{M}_{exp} come out to be 1.79×10^{-12} and $7.18 \times 10^{-11} \text{ g cm}^{-2} \text{ s}^{-1}$ for the 100×Solar and 1000×Solar cases, respectively, which are 9.66 and 380 times larger than those of \dot{M} that we used in § 3.3.

Figure 22 shows the transmission spectrum models for the hazy 100×Solar atmosphere calculated with \dot{M}_{exp} (yellow line) and \dot{M} (red thick line, same as the red thick line in Fig. 9) and the hazy 1000×Solar atmosphere calculated with \dot{M}_{exp} (light-blue line) and \dot{M} (purple thick line, same as the purple thick line in Fig. 9). The transmission spectra for the corresponding haze-free atmospheres are also plotted with the red thin line (same as the red thin line in Fig. 9) and purple thin line (same as the purple thin line in Fig. 9), respectively.

The transmission spectra for \dot{M}_{exp} turn out to be more featureless relative to those for \dot{M} . This is because \dot{M}_{exp} is much higher than \dot{M} . Especially, the

spectrum for the hazy 1000×Solar atmosphere calculated with \dot{M}_{exp} is flat in almost the entire wavelength region. We consider that the several factors are responsible for the much higher values of \dot{M}_{exp} than those of \dot{M} . First, the experiments include much more complex chemistry than our photochemical simulations, while we assume 100% conversion efficiency of forming haze from the photodissociation of our relatively limited number of haze precursors to haze monomers. Recent laboratory experiments identified some other potential key precursors such as CH₂NH and HCHO in addition to the species assumed in our simulations, CH₄, HCN, and C₂H₂ (He et al. 2019). Our limited number of haze precursors can make \dot{M} smaller than \dot{M}_{exp} , while \dot{M} can be overestimated since the 100% conversion efficiency is obviously unlikely to be achievable. On the other hand, the vertical photon-shielding effect by the other molecules, existing at higher altitudes than the hydrocarbons, is not considered in the experiments, while considered in our simulations. This can also make \dot{M}_{exp} higher. Moreover, although we assume the linear-dependence of the photodissociation rates of the haze precursors on the incident UV flux, our results in § 3.2 imply that the relationship is slightly weaker than the linear-one, while the dependence is not monotonic. This can be also responsible for the higher values of \dot{M}_{exp} .

As mentioned in § 3.3, recent laboratory experiments implied that not only the photodissociation of hydrocarbons, but also that of CO, CO₂, and H₂O can lead to the formation of haze, implying the existence of multiple formation pathways (Hörst et al. 2018; He et al. 2019). If we also include the photodissociation rates of CO, CO₂, and H₂O, the total monomer production rates become 1.93×10^{-10} , 3.08×10^{-10} , 3.50×10^{-10} , and $4.07 \times 10^{-10} \text{ g cm}^{-2} \text{ s}^{-1}$ for the 1, 10, 100, and 1000×Solar cases, respectively, and thus larger for higher metallicities. As for C/O ratio, those values become 1.93×10^{-10} , 1.81×10^{-10} , 1.53×10^{-10} , and $1.03 \times 10^{-10} \text{ g cm}^{-2} \text{ s}^{-1}$ for the cases of C/O = 0.5, 1, 10, and 1000, respectively, and thus slightly smaller for higher values of C/O ratio. Finally for temperature, those values become 1.93×10^{-10} and $2.51 \times 10^{-10} \text{ g cm}^{-2} \text{ s}^{-1}$ for the cases of $T_{\text{irr}} = 790$ and 1290 K, respectively, and thus larger for higher temperatures. These opposite dependence from our results for all of the above three parameters, metallicity, C/O ratio, and temperature, come from the fact that CO, CO₂, and H₂O absorb much more photons than the hydrocarbons we have assumed as the precursors and also, their abundances are larger for the higher metallicities and temperatures, and smaller for the higher C/O ratios. However, key haze precursors have not been fully understood and are still in debate.

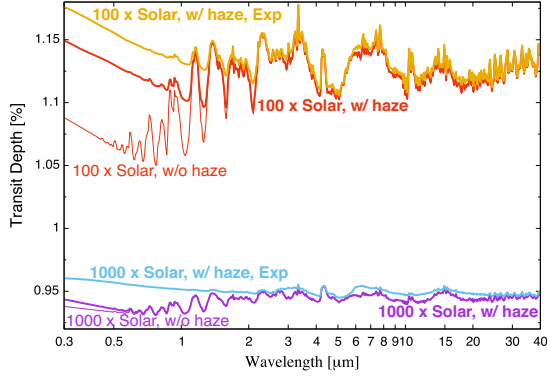


Figure 22. Transmission spectrum models for the hazy $100 \times$ Solar atmospheres calculated with \dot{M}_{exp} (yellow line) and \dot{M} (red thick line, same as the red thick line in Fig. 9) and $1000 \times$ Solar atmospheres calculated with \dot{M}_{exp} (light-blue line) and \dot{M} (purple thick line, same as the purple thick line in Fig. 9). See the text for the definition of each quantity. The transmission spectrum for the $100 \times$ Solar and $1000 \times$ Solar atmospheres without haze are also plotted in red thin line (same as the red thin line in Fig. 9) and purple thin line (same as the purple thin line in Fig. 9), respectively. Note that the transmission spectrum models are smoothed for clarity.

In addition, the conversion efficiency of forming haze from the photodissociation of each precursor is still quite uncertain and the 100% conversion efficiency we have assumed here is obviously overestimated. In summary, to gain a deeper understanding of haze production, we need more data from laboratory experiments obviously, but, furthermore, incorporate them correctly in atmospheric models.

4.3. Comparison with Previous Studies

There are some parameter studies that explored transmission spectra of hydrogen-rich atmospheres with focus on the effects of haze or cloud particles.

First, while we have focused on super-Earths with moderate temperatures in this study, considering hot Jupiters such as HD 209458b and HD 189733b, Lavvas & Koskinen (2017) calculated photochemistry and microphysics of haze particles, modeled the transmission spectra, and compared them with the observed spectra. They also explored the dependence of the transmission spectra on the poorly constrained parameters including the monomer production rate, eddy diffusion, and temperature-pressure profile. They found that higher monomer production rates led to the formation of larger particles, yielding flatter transmission spectra, which is consistent with our finding in Paper I. In addition, they found that efficient eddy diffusion hampers collision between particles, making the atmosphere optically thin, which is also consistent with our results

in § 3.5. Finally, as for the temperature-pressure profile, they showed that the resultant transmission spectra for the hotter and cooler temperature-pressure profiles were almost similar to each other, in contrast to our finding that the transmission spectrum for the hotter atmosphere is less affected by haze and has more prominent absorption features (see § 3.6). Such a difference in temperature dependence of transmission spectrum comes from the fact that they assumed the fixed value of the monomer production rate regardless of temperature, whereas we have determined it from the temperature-dependent photodissociation rates of the hydrocarbons.

Regarding condensation clouds, the dependence of atmospheric transmission spectra on eddy diffusion have been investigated by Gao & Benneke (2018) and Ormel & Min (2019). Whereas the atmosphere with the photochemical haze becomes less thick and the resultant transmission spectrum has more prominent molecular-absorption features for higher values of eddy diffusion coefficient (see § 3.5), the amount of condensation clouds increases with increasing eddy diffusion coefficient (Gao & Benneke 2018; Ormel & Min 2019). Such a difference comes from the fact that haze particles are formed in upper atmospheric regions and transported downward, while condensation clouds are formed in lower atmospheric regions and transported upward. This implies that both haze and condensation clouds being considered, efficient eddy diffusion does not necessarily reduce the optical thickness of the atmosphere as we have shown in §3.5. Taking their coexistence in the atmosphere into account is one of our important future studies.

4.4. Caveats

4.4.1. Monomer Radius

While we have adopted 1 nm for the monomer radius following some previous studies (e.g., Toon et al. 1992; Lavvas & Koskinen 2017) in this paper, we have confirmed that it has a little effect on the transmission spectrum. Indeed, calculating the vertical distributions of haze particles with monomer radii of 10 and 20 nm, we have found that all the average radii, number densities, and total mass density agree fairly well with those in the fiducial 1-nm case in the lower atmosphere of $P \gtrsim 10^{-6}$ bar, so that the resultant transmission spectra are almost similar as shown in Figure 23. In the upper atmosphere ($P \lesssim 10^{-6}$ bar), where the particle sizes are still small and affected by the initial monomer size, the total mass densities for the 10 and 20-nm cases are smaller by about an order of magnitude because the larger particles fall more rapidly. However, this differ-

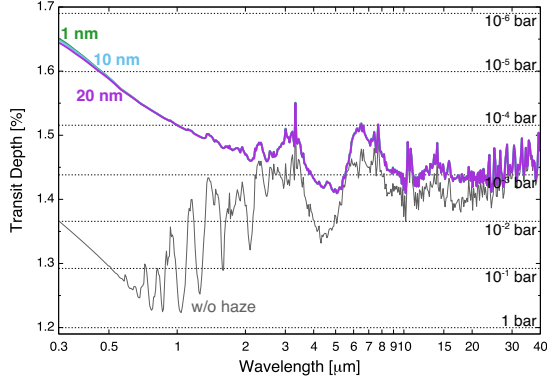


Figure 23. Transmission spectrum models for the atmosphere with haze for the three different values of the monomer radius, 1 nm (green line, same as the green line in Fig. 5), 10 nm (light-blue line), and 20 nm (purple line). The transmission spectrum for the atmosphere without haze is also plotted (black line, same as the black line in Fig. 5). As in Fig. 5, horizontal dotted lines represent the transit depths corresponding to the pressure levels from 1×10^{-6} bar to 1 bar. Note that the transmission spectrum models are smoothed for clarity.

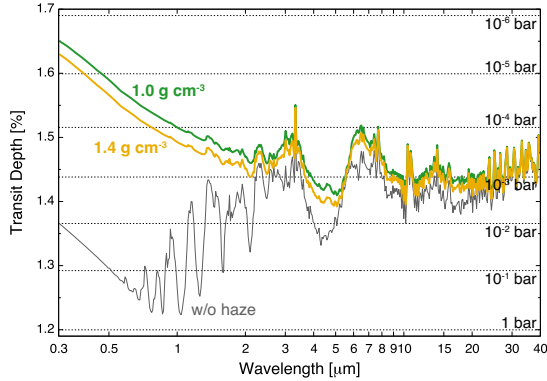


Figure 24. Transmission spectrum models for the atmosphere with haze for the two different values of the material density, 1.0 g cm^{-3} (green line, same as the green line in Fig. 5) and 1.4 g cm^{-3} (orange line). The transmission spectrum for the atmosphere without haze is also plotted (black line, same as the black line in Fig. 5). As in Fig. 5, horizontal dotted lines represent the transit depths corresponding to the pressure levels from 1×10^{-6} bar to 1 bar. Note that the transmission spectrum models are smoothed for clarity.

ence occurs high enough in the upper atmosphere that it has little effect on the resultant transmission spectrum.

4.4.2. Material Density

In this study, we have adopted 1.0 g cm^{-3} for the value of the material density of haze particles as the widely used value for the microphysical models of Titan’s haze (e.g., Toon et al. 1992; Lavvas et al. 2011). However, recent laboratory experiments of Titan’s haze analogues

measured the slightly higher material density of $1.3\text{--}1.4 \text{ g cm}^{-3}$ (Imanaka et al. 2012; He et al. 2017). Thus, we simulate the transmission spectrum model for the atmosphere with haze, adopting the value of 1.4 g cm^{-3} for the material density, which is shown in Figure 24. Since the particle sedimentation velocity is linearly proportional to the material density (see Eq. (13) of Paper I), haze particles fall more rapidly for the larger material density case and thus the atmosphere becomes slightly less optically-thick.

4.4.3. Fluffy Particles

In this study, we have modeled particle growth assuming compact spherical particles. For the Titan’s atmosphere, observation suggests that the haze particles have a fractal structure with a fractal dimension of ~ 2 (Cabane et al. 1992, 1993; Rannou et al. 1995, 1997). Since the sedimentation velocity of such fluffy particles is small and their collisional cross section is large compared to that of spherical compact ones with the same mass, atmospheric transmission spectra with the former would be flatter than those with the latter as recently shown by Adams et al. (2019). This effect will be explored in detail in our forthcoming papers.

5. SUMMARY AND CONCLUSIONS

In this study, we have investigated transmission spectra of atmospheres of close-in warm ($\lesssim 1000 \text{ K}$) exoplanets with hydrocarbon haze for wide ranges of the model parameters, namely, UV irradiation intensity, metallicity, carbon-to-oxygen ratio (C/O), eddy diffusion coefficient, and atmospheric temperature. We have focused on the vertical distributions of the haze particles and gaseous species. In particular, in contrast to previous studies including Paper I, we have made a more realistic assumption that the monomer production rate is equal to be the sum of the photodissociation rates of the hydrocarbons, CH_4 , HCN , and C_2H_2 .

We have found that differences in UV irradiation intensity yields a diversity of transmission spectra, which are observationally suggested (see § 3.2). The photodissociation rates of the hydrocarbons depend relatively weakly on the UV irradiation intensity with the proportion of the incoming photons used for the photodissociation of the haze precursors decreasing with increasing UV flux. This is due to an enhanced photon-shielding effect by CO and O_2 , which exist at higher altitudes than the hydrocarbons.

As for metallicity, we have demonstrated that the photodissociation rates of the hydrocarbons (and thus the monomer production rates) are basically smaller for higher metallicities in spite of their increased abundances (see § 3.3). This is due to an enhanced photon-

shielding effect by the major photon absorbers, H_2O , CO , CO_2 , and O_2 , existing at higher altitudes than the hydrocarbons. However, since the atmospheric scale height is also smaller for higher metallicities, the metallicity affects strengths of absorption features in the transmission spectra in a somewhat complicated way: Moderate metallicities (such as 100 times the solar metallicity) result in large absorption features at short wavelengths ($\lesssim 2\text{--}3\ \mu\text{m}$), while lower metallicities result in larger ones at longer wavelengths ($\gtrsim 2\text{--}3\ \mu\text{m}$). While recent chamber-experiments for production of hydrocarbons demonstrated higher production rates in higher metallicity gases (He et al. 2018a; Hörst et al. 2018; He et al. 2018b), we warn that when applying to the real atmospheres, we also need to consider such a shielding effect by the other molecules, which we have found is larger for higher metallicity.

Regarding carbon-to-oxygen ratio (see § 3.4), higher values of C/O generally yield larger photodissociation rates of the hydrocarbons, because of the decreased abundances of the major photon-shielding molecules H_2O , CO , CO_2 , and O_2 . As a result, the molecular absorption features in the transmission spectrum become less prominent with increasing C/O. However, the transmission spectrum never becomes completely flat, because the absorption features of haze particles remain even for extremely high C/O ($= 10^{10}$). This is because the total photodissociation rates of hydrocarbons are limited not by the amount of carbon, but by the incoming photon flux.

We have demonstrated that the efficient eddy diffusion yields a steep Rayleigh-scattering slope in the optical and more prominent molecular-absorption features (see § 3.5). Such a dependence is opposite to that for the case of condensation clouds (Gao & Benneke 2018; Ormel & Min 2019). This is because haze particles are formed at high altitudes and transported downward, while condensation clouds are formed at relatively low altitudes and transported upward.

Finally, we have found that higher temperature results in smaller photodissociation rates of the hydrocarbons since CO rather than CH_4 becomes the dominant carbon-bearing species at high temperatures. Thus, the resultant spectrum for the higher atmospheric temperature has more distinct molecular absorption features.

In conclusion, detection of molecular absorption features in hazy atmospheres favors planets with lower

incoming UV flux and higher temperature. As for metallicity, we have revealed its somewhat complicated effect on transmission spectra. From this, we warn that the featureless spectra recently observed for some exoplanets do not necessarily indicate high atmospheric metallicities. As an observational strategy for obtaining constraints on atmospheric metallicities of many exoplanets expected to be discovered by TESS (Ricker et al. 2014) and PLATO (Rauer et al. 2014), multi-color broad-band observations especially at optical wavelengths with ground-based telescopes such as MuSCATs (Narita et al. 2015; Narita et al. 2018) are useful to select targets for further detailed observations, since atmospheres showing steep spectral slopes in the optical are likely to show strong absorption features in the infrared. However, in order to put more precise constraints on atmospheric metallicity by breaking the degeneracy of metallicity with eddy diffusion coefficient, we claim that it is necessary to measure the strength of absorption features in the infrared, where the contribution of haze is small. For this purpose, of great importance are space-based telescopes feasible for observations at mid-infrared wavelengths such as JWST (Gardner et al. 2006) and those dedicated to exoplanet chemical characterization such as ARIEL (Tinetti et al. 2018).

We would like to express special thanks to the following people. N. Narita and A. Fukui motivated us to work on this study and gave fruitful suggestions through observational collaboration. Advice and comments from Y. Sekine and S. Okuzumi were great help in modeling the properties of haze particles. We thank the anonymous referee for his/her careful reading and constructive comments, which helped us improve this paper greatly. Y.K. is supported by the Grant-in-Aid for JSPS Fellow (JSPS KAKENHI No.15J08463), Leading Graduate Course for Frontiers of Mathematical Sciences and Physics, Grant-in-Aid for Scientific Research (A) (JSPS KAKENHI No.15H02065), and the European Union’s Horizon 2020 Research and Innovation Programme under Grant Agreement 776403. M. I. is also supported by the Astrobiology Center Program of National Institutes of Natural Sciences (NINS) (No. AB291004) and JSPS Core-to-Core Program International Network of Planetary Sciences. This work has made use of the MUSCLES Treasury Survey High-Level Science Products (doi:10.17909/T9DG6F).

REFERENCES

- Adams, D., Gao, P., de Pater, I., & Morley, C. V. 2019, *ApJ*, 874, 61, doi: [10.3847/1538-4357/ab074c](https://doi.org/10.3847/1538-4357/ab074c)
- Anglada-Escudé, G., Rojas-Ayala, B., Boss, A. P., Weinberger, A. J., & Lloyd, J. P. 2013, *A&A*, 551, A48, doi: [10.1051/0004-6361/201219250](https://doi.org/10.1051/0004-6361/201219250)

- Binney, J., & Merrifield, M. 1998, *Galactic Astronomy*
- Bohren, C. F., & Huffman, D. R. 2004, *Absorption and Scattering of Light by Small Particles* (Weinheim: Wiley-VCH).
- [OPAC]https://opac.dl.itc.u-tokyo.ac.jp/opac/opac_details.cgi?lang=0&bbid=2003403325&code=11JWebcatPlus
- Brown, T. M. 2001, *ApJ*, 553, 1006, doi: [10.1086/320950](https://doi.org/10.1086/320950)
- Cabane, M., Chassefiere, E., & Israel, G. 1992, *Icarus*, 96, 176, doi: [10.1016/0019-1035\(92\)90071-E](https://doi.org/10.1016/0019-1035(92)90071-E)
- Cabane, M., Rannou, P., Chassefiere, E., & Israel, G. 1993, *Planet. Space Sci.*, 41, 257, doi: [10.1016/0032-0633\(93\)90021-S](https://doi.org/10.1016/0032-0633(93)90021-S)
- Crossfield, I. J. M., & Kreidberg, L. 2017, *AJ*, 154, 261, doi: [10.3847/1538-3881/aa9279](https://doi.org/10.3847/1538-3881/aa9279)
- Ehrenreich, D., Bonfils, X., Lovis, C., et al. 2014, *A&A*, 570, A89, doi: [10.1051/0004-6361/201423809](https://doi.org/10.1051/0004-6361/201423809)
- France, K., Parke Loyd, R. O., Youngblood, A., et al. 2016, *ApJ*, 820, 89, doi: [10.3847/0004-637X/820/2/89](https://doi.org/10.3847/0004-637X/820/2/89)
- Fukui, A., Kawashima, Y., Ikoma, M., et al. 2014, *ApJ*, 790, 108, doi: [10.1088/0004-637X/790/2/108](https://doi.org/10.1088/0004-637X/790/2/108)
- Fukui, A., Narita, N., Kawashima, Y., et al. 2016, *ApJ*, 819, 27, doi: [10.3847/0004-637X/819/1/27](https://doi.org/10.3847/0004-637X/819/1/27)
- Gao, P., & Benneke, B. 2018, *ApJ*, 863, 165, doi: [10.3847/1538-4357/aad461](https://doi.org/10.3847/1538-4357/aad461)
- Gardner, J. P., Mather, J. C., Clampin, M., et al. 2006, *SSRv*, 123, 485, doi: [10.1007/s11214-006-8315-7](https://doi.org/10.1007/s11214-006-8315-7)
- Guillot, T. 2010, *A&A*, 520, A27, doi: [10.1051/0004-6361/200913396](https://doi.org/10.1051/0004-6361/200913396)
- He, C., Hörst, S. M., Riemer, S., et al. 2017, *ApJL*, 841, L31, doi: [10.3847/2041-8213/aa74cc](https://doi.org/10.3847/2041-8213/aa74cc)
- He, C., Hörst, S. M., Lewis, N. K., et al. 2018a, *ApJL*, 856, L3, doi: [10.3847/2041-8213/aab42b](https://doi.org/10.3847/2041-8213/aab42b)
- . 2018b, *AJ*, 156, 38, doi: [10.3847/1538-3881/aac883](https://doi.org/10.3847/1538-3881/aac883)
- He, C., Hrst, S. M., Lewis, N. K., et al. 2019, *ACS Earth and Space Chemistry*, 3, 39, doi: [10.1021/acsearthspacechem.8b00133](https://doi.org/10.1021/acsearthspacechem.8b00133)
- Heng, K. 2016, *ApJL*, 826, L16, doi: [10.3847/2041-8205/826/1/L16](https://doi.org/10.3847/2041-8205/826/1/L16)
- Heng, K., & Kitzmann, D. 2017, *MNRAS*, 470, 2972, doi: [10.1093/mnras/stx1453](https://doi.org/10.1093/mnras/stx1453)
- Hörst, S. M., He, C., Lewis, N. K., et al. 2018, *Nature Astronomy*, 2, 303, doi: [10.1038/s41550-018-0397-0](https://doi.org/10.1038/s41550-018-0397-0)
- Howe, A. R., & Burrows, A. S. 2012, *ApJ*, 756, 176, doi: [10.1088/0004-637X/756/2/176](https://doi.org/10.1088/0004-637X/756/2/176)
- Imanaka, H., Cruikshank, D. P., Khare, B. N., & McKay, C. P. 2012, *Icarus*, 218, 247, doi: [10.1016/j.icarus.2011.11.018](https://doi.org/10.1016/j.icarus.2011.11.018)
- Kawashima, Y., Hu, R., & Ikoma, M. 2019, *ApJL*, in press
- Kawashima, Y., & Ikoma, M. 2018, *ApJ*, 853, 7, doi: [10.3847/1538-4357/aaa0c5](https://doi.org/10.3847/1538-4357/aaa0c5)
- Khare, B. N., Sagan, C., Arakawa, E. T., et al. 1984, *Icarus*, 60, 127, doi: [10.1016/0019-1035\(84\)90142-8](https://doi.org/10.1016/0019-1035(84)90142-8)
- Kreidberg, L., Bean, J. L., Désert, J.-M., et al. 2014, *Nature*, 505, 69, doi: [10.1038/nature12888](https://doi.org/10.1038/nature12888)
- Lavvas, P., & Koskinen, T. 2017, *ApJ*, 847, 32, doi: [10.3847/1538-4357/aa88ce](https://doi.org/10.3847/1538-4357/aa88ce)
- Lavvas, P., Sander, M., Kraft, M., & Imanaka, H. 2011, *ApJ*, 728, 80, doi: [10.1088/0004-637X/728/2/80](https://doi.org/10.1088/0004-637X/728/2/80)
- Lavvas, P., Yelle, R. V., & Griffith, C. A. 2010, *Icarus*, 210, 832, doi: [10.1016/j.icarus.2010.07.025](https://doi.org/10.1016/j.icarus.2010.07.025)
- Lodders, K. 2003, *ApJ*, 591, 1220, doi: [10.1086/375492](https://doi.org/10.1086/375492)
- Loyd, R. O. P., France, K., Youngblood, A., et al. 2016, *ApJ*, 824, 102, doi: [10.3847/0004-637X/824/2/102](https://doi.org/10.3847/0004-637X/824/2/102)
- McKay, C. P., Coustenis, A., Samuelson, R. E., et al. 2001, *Planet. Space Sci.*, 49, 79, doi: [10.1016/S0032-0633\(00\)00051-9](https://doi.org/10.1016/S0032-0633(00)00051-9)
- Miller-Ricci, E., & Fortney, J. J. 2010, *ApJL*, 716, L74, doi: [10.1088/2041-8205/716/1/L74](https://doi.org/10.1088/2041-8205/716/1/L74)
- Morley, C. V., Fortney, J. J., Kempton, E. M.-R., et al. 2013, *ApJ*, 775, 33, doi: [10.1088/0004-637X/775/1/33](https://doi.org/10.1088/0004-637X/775/1/33)
- Narita, N., Fukui, A., Kusakabe, N., et al. 2015, *Journal of Astronomical Telescopes, Instruments, and Systems*, 1, 045001, doi: [10.1117/1.JATIS.1.4.045001](https://doi.org/10.1117/1.JATIS.1.4.045001)
- Narita, N., Fukui, A., Kusakabe, N., et al. 2018, *Journal of Astronomical Telescopes, Instruments, and Systems*, 5, 015001
- Ohno, K., & Okuzumi, S. 2018, *ApJ*, 859, 34, doi: [10.3847/1538-4357/aabee3](https://doi.org/10.3847/1538-4357/aabee3)
- Ormel, C. W., & Min, M. 2019, *A&A*, 622, A121, doi: [10.1051/0004-6361/201833678](https://doi.org/10.1051/0004-6361/201833678)
- Powell, D., Zhang, X., Gao, P., & Parmentier, V. 2018, *ApJ*, 860, 18, doi: [10.3847/1538-4357/aac215](https://doi.org/10.3847/1538-4357/aac215)
- Rannou, P., Cabane, M., Botet, R., & Chassefière, E. 1997, *J. Geophys. Res.*, 102, 10997, doi: [10.1029/97JE00719](https://doi.org/10.1029/97JE00719)
- Rannou, P., Cabane, M., Chassefiere, E., et al. 1995, *Icarus*, 118, 355, doi: [10.1006/icar.1995.1196](https://doi.org/10.1006/icar.1995.1196)
- Rauer, H., Catala, C., Aerts, C., et al. 2014, *Experimental Astronomy*, 38, 249, doi: [10.1007/s10686-014-9383-4](https://doi.org/10.1007/s10686-014-9383-4)
- Ricker, G. R., Winn, J. N., Vanderspek, R., et al. 2014, in *Proc. SPIE, Vol. 9143, Space Telescopes and Instrumentation 2014: Optical, Infrared, and Millimeter Wave*, 914320
- Rothman, L. S., Gordon, I. E., Babikov, Y., et al. 2013, *JQSRT*, 130, 4, doi: [10.1016/j.jqsrt.2013.07.002](https://doi.org/10.1016/j.jqsrt.2013.07.002)
- Sing, D. K., Fortney, J. J., Nikolov, N., et al. 2016, *Nature*, 529, 59, doi: [10.1038/nature16068](https://doi.org/10.1038/nature16068)
- Stevenson, K. B. 2016, *ApJL*, 817, L16, doi: [10.3847/2041-8205/817/2/L16](https://doi.org/10.3847/2041-8205/817/2/L16)

- Tinetti, G., Drossart, P., Eccleston, P., et al. 2018, *Experimental Astronomy*, 46, 135, doi: [10.1007/s10686-018-9598-x](https://doi.org/10.1007/s10686-018-9598-x)
- Toon, O. B., McKay, C. P., Griffith, C. A., & Turco, R. P. 1992, *Icarus*, 95, 24, doi: [10.1016/0019-1035\(92\)90188-D](https://doi.org/10.1016/0019-1035(92)90188-D)
- Trainer, M. G., Pavlov, A. A., Dewitt, H. L., et al. 2006, *Proceedings of the National Academy of Science*, 103, 18035, doi: [10.1073/pnas.0608561103](https://doi.org/10.1073/pnas.0608561103)
- Youngblood, A., France, K., Parke Loyd, R. O., et al. 2016, *ApJ*, 824, 101, doi: [10.3847/0004-637X/824/2/101](https://doi.org/10.3847/0004-637X/824/2/101)